This is a peer-reviewed, accepted author manuscript of the following research article: Dodo, K, Tipping, WJ, Yamakoshi, H, Egoshi, S, Kubo, T, Kumamoto, Y, Faulds, K, Graham, D, Fujita, K & Sodeoka, M 2025, 'Alkyne-tag Raman imaging and sensing of bioactive compounds', Nature Reviews Methods Primers, vol. 5, no. 1, 20. https://doi.org/10.1038/s43586-025-00389-9

Alkyne-tag Raman imaging and sensing of bioactive compounds

Kosuke Dodo[1]*, William J. Tipping[2], Hiroyuki Yamakoshi[3], Syusuke Egoshi[1], Toshiki Kubo[4,5], Yasuaki Kumamoto[4,6], Karen Faulds[2], Duncan Graham[2]*, Katsumasa Fujita[4,6]* and Mikiko Sodeoka[1]*

[1]RIKEN Center for Sustainable Resource Science, Wako, Saitama, Japan

[2]Department of Pure and Applied Chemistry, Technology and Innovative Centre, University of Strathclyde, Glasgow, UK

[3]Graduate School of Pharmaceutical Sciences, Tohoku University, Sendai, Japan

[4]Department of Applied Physics, Graduate School of Engineering, Osaka University, Suita, Osaka, Japan

[5]Department of Dermatology, Graduate School of Medicine, Osaka University, Suita, Osaka, Japan

[5]Institute for Open and Transdisciplinary Research Initiatives, Osaka University, Osaka, Japan

*email: dodo@riken.jp, duncan.graham@strath.ac.uk, fujita@ap.eng.osaka-u.ac.jp, sodeoka@riken.jp

Abstract

An alkyne is an unsaturated hydrocarbon that is characterized by the presence of at least one C≡C bond. Alkyne groups generate a strong Raman peak in the cellular silent region, a region between 1800 and 2800 cm^{-1} where endogenous molecules do not produce a Raman signal. As a result, alkynes are regularly used as tags to label and visualize small molecules in live cells using Raman microscopy, a method referred to as alkyne-tag Raman imaging (ATRI). ATRI has been applied to various compounds to enable their cellular localization and recently, alkyne-tagged compounds have been used as Raman sensors to detect intracellular biomolecules, such as metal ions or reactive oxygen species. ATRI has unique advantages over existing methods for localizing small molecules intracellularly, such as enabling super-multiplex detection and incurring a smaller impact on labelled compounds. In this Primer, we describe the principles and key techniques involve in ATRI, including the design of alkyne-tagged molecules, sample preparation, and the set-up of Raman microscopes. We showcase the demonstration and application of ATRI, encompassing the development of responsive alkyne-tagged compounds for sensing biomolecules. Finally, we discuss the limitations and potential applications of ATRI, shedding light on the future possibilities of this method.

[H1] Introduction

Raman imaging is a technique that generates images of a substance and derives information on its composition using the inelastic scattering of light, known as Raman scattering[1]. Raman scattering has a different energy and thus wavelength from the incident light source, with the energy difference depending on molecular vibrations correlating to the chemical structure and environment of the sample molecule. Spectral analysis of Raman scattering gives a Raman spectrum that contains molecular vibrational information about the sample. By using a Raman microscope, Raman spectra can be measured at specific locations within or across a whole sample of interest and the distribution of a specific molecule can be visualized based on a specific Raman signal, which is the basis of Raman imaging.

In principle, the Raman signal is very weak compared with fluorescence. However, a major advantage of Raman imaging is that it can detect abundant biomolecules based on innate Raman signals. By contrast, fluorescence imaging detects fluorescent molecules with very high sensitivity, although it requires fluorescence labelling of the target molecule to do so. Label-free Raman imaging has been applied to visualize endogenous biomolecules, such as lipids, proteins, and nucleic acids, that cannot be achieved by fluorescence imaging.

In the last decade, the concept of Raman tagging has been established, whereby the introduction of a Raman-active molecular group into the molecular structure enables the detection of the labelled molecule via the tag group, which is spectrally resolved from endogenous Raman peaks of the sample. The application of Raman tagging has dramatically broadened the use of Raman imaging for biological studies. Bioactive compounds, such as pharmaceuticals, exhibit their biological activity by interacting with their target molecules in cells. The subcellular distribution of a bioactive compound reflects its site of action and provides useful information. However, it is often difficult to apply fluorescent imaging for visualizing bioactive compound in live cells as many compounds are not inherently fluorescent and introduction of fluorescent tags often changes the properties of the compound due to their large molecular size. Alkyne-tag Raman imaging (ATRI) has been developed to overcome this problem as a new imaging method for small molecules in live cells[2,3]; in this method, the target molecule is labelled with an alkyne tag **[G]** and detected by Raman microscopy. An alkyne is a small functional group (MW: 25 g/mol) compared with a fluorescent group and shows an intense peak in the Raman-silent region of the cellular Raman spectrum (1800—2800 cm^{-1}). Therefore, an alkyne can be attached to a target compound, maintaining bioactivity, and used as a detection tag for Raman imaging. By using this method, the cellular localization of bioactive compounds can be examined for the elucidation of previously unknown mechanisms of action. Furthermore, the subcellular accumulation of various molecules can be quantified, and the efficiency of cellular uptake — an important factor of bioactivity — can be estimated. ATRI has contributed to various research fields including pharmaceutical sciences and chemical biology research[4,5].

The design of alkyne-tagged molecules is important for ATRI methods as the molecular structure conjugated to the alkyne tag affects the strength of its Raman signal. Installation of chemically reactive groups in conjugation with the alkyne tag can be used to produce sensors that respond to environmental stimuli, for example local pH changes[6,7]. Raman dyes[8,9] showing strong Raman signals in the cellular-silent region can be applied to the labelling of proteins or cells instead of fluorescent dyes. The high spectral resolution of Raman microscopy has realized super-multiplex imaging in a way that fluorescent microscopy could not. The Raman dyes offer 100-fold higher wavenumber resolution than fluorescent dyes. Recently, Raman dyes were applied to Raman sensors, which can detect multiple enzyme activities in cells[10] and in vivo[11]. Further applications of Raman sensors and dyes are expected to transform the biological studies that currently depend on fluorescence.

Due to the weakness of Raman signal, it had been difficult to apply Raman spectroscopy to biological studies. However, technical progress, such as the development of high-powered lasers, highly sensitive detectors, and optical filters, have enabled Raman imaging of biological samples. Furthermore, new modalities of Raman microscopes have broadened the range of applications, such as high-speed Raman imaging[12]. In particular, the combination of alkyne tags and stimulated Raman scattering (SRS) microscopy[13] has opened new avenues for biological application of Raman imaging[14]. In this Primer, we discuss the Raman imaging of alkyne-tagged small molecules. We describe key points such as the setup of Raman microscopes for ATRI, the design of alkyne-tagged molecules, sample preparation, and data analysis (FIG. 1). We also showcase several successful examples and discuss the future potential of this method.

[H1] Experimentation

Spontaneous Raman microscopy and stimulated Raman scattering (SRS) microscopy are the main modes used for ATRI. FIG. 2a shows the schematic of energy diagrams of Raman scattering, resonant Raman scattering, and SRS. Raman scattering is spontaneous emission from a molecule excited by the incident laser from the ground electric state to a virtual excited state. When the energy of the incident light is close to an electric excited state, a resonant effect occurs and the scattering cross-section increases, which is referred to as resonant Raman scattering. SRS is stimulated emission induced by a stokes beam from the molecule excited by the pump beam. The principle and setup for these systems is described below.

[H2] Spontaneous Raman microscopy

In spontaneous Raman imaging, Raman scattering is induced by a focused excitation light source, typically a narrow-band continuous wave (CW) laser. The Raman scattering from a chemical bond

exhibits a specific wavelength shift relative to the excitation wavelength, corresponding to the energy of the molecular vibration. Biological samples contain various molecules with distinct chemical bonds, leading to Raman scattering at different wavelengths. Spectral detection is used to obtain information about various molecular vibrations from samples, including signals from the cell fingerprint region (500–1800cm^{-1}) and the high-wavenumber region (2800–3000cm^{-1}). A CCD ditector is typically used for the spectral detection. In a simple point-scanning setup, the laser beam is scanned over a region of interest to generate a hyperspectral Raman image (FIG 2b). In slit-scanning setups, the excitation light is focused in a line-shape onto samples and the spectra of the induced Raman scattering are simultaneously imaged using a 2D image sensor (FIG 2c). This simultaneous detection scheme enables a Raman image to be obtained through scanning the laser over the surface of the sample in a single direction, which results in a few-hundred-times higher temporal resolution than a point-scanning system. This feature makes it more suited to observing live samples than point-scanning approaches. Both point- and slit-scanning confocal Raman microscopes have been used for alkyne-tag spontaneous Raman scattering[2,3,15,16]. FIG. 2d shows and a typical optical setup of a line-illumination spontaneous Raman microscope.

Spontaneous Raman scattering can be enhanced under the presence of resonance between the excitation and the electric excited state of molecules by a few orders of magnitude[17]. Nanomaterials that exhibit a localised surface plasmon resonance **[G]** (LSPR), typically a roughened metal surface, induce electromagnetic enhancement of the Raman scattering signal in the order of 10^4 to 10^8 compared to spontaneous Raman scattering[18]; this process is called surface-enhanced Raman scattering (SERS) and has successfully been implemented in ATRI[19-26].

[H2] Stimulated Raman scattering (SRS) microscopy

In SRS microscopy, two ultrashort-pulse lasers are used as the pump and Stokes beams. To induce SRS, the two beams are focused on the sample so that they overlap spatially and temporally. The molecular vibrational signal is selectively detected when its energy matches the wavelength difference between the pump and Stokes beams, manifesting as stimulated Raman loss (SRL) or stimulated Raman gain (SRG) owing to energy exchange between the two beams through the vibrational excited state (FIG 2e). Therefore, the detected signal is basically limited in narrow wavenumber region including single Raman band, and single channel photo detector. The excitation cross-section **[G]** of SRS is 5-to-6 orders of magnitude higher than spontaneous Raman scattering, enabling imaging speeds comparable to fluorescence confocal microscopy. FIG. 2f shows an example of a typical optical setup for SRS microscopy[27-29].

To perform multiband SRS imaging, the optics need to be modified. There are several methods available for detecting multiple Raman bands in an SRS microscope. Sweeping the wavelength

of one of the lasers is a simple method, tuning the wavelength difference between the two beams and the target Raman band[30,31]. Introducing a pulse shaper is another method, which is composed of 4-f optics with one or a pair of gratings and a spatial filter, typically a spatial light modulator (SLM) or a slit placed on a motorized stage[32-35]. A pulse shaper enables stretching either or both of the two beams in space depending on the light wavelength and picking up specific wavelengths by the spatial filter to selectively realize wavelength differences of the beams and the detection of multiple target Raman bands of interest. In spectral focusing[36-40] two laser beams are chirped by dispersive optics and a temporal delay is applied on one of the beam to control the timing of arrival at sample position. Depending on the applied time delay, the wavelength difference is changed. Therefore, by scanning the time delay, multiple Raman bands are obtained. Parallel multi-mode excitation and detection schemes[41-47] typically hire a broadband and a narrowband laser for the two beams, and a multi-channel detector to detect multiple Raman band signals simultaneously. Another option is to modulate the beams with different wavelengths of the broadband light source at different frequencies, and then use lock-in detection to distinguish different Raman band signals. Femtosecond pulsed lasers can be used to replace one or both light sources as broadband light source for implementing these methods.

[H2] Comparison of Raman microscopies for ATRI

Table 1 provides a brief comparison of the specification of spontaneous Raman microscopy and SRS microscopy. Spontaneous Raman microscopy offers a broad spectral detection bandwidth and higher spectral resolution, allowing for the simultaneous detection of Raman signals from intrinsic biological molecules in both fingerprint and high-wavenumber regions, as well as from Raman probes. Although the acquisition speed of Raman spectral imaging can restrict the throughput of the technique to the order of minutes per cell, the spectral coverage and resolution is currently superior to that which can be achieved by SRS. Most commercially available spontaneous Raman microscopes can provide spectral resolution at < 1 cm^{-1}, which is optimal for the analysis of ratiometric Raman sensors where the shifting of the alkyne reporter ($\Delta\nu$) can be < 10 cm^{-1}.

By contrast, SRS microscopy — though limited by a relatively narrow spectral bandwidth — enables faster imaging, which is suitable for visualizing single or multiple Raman probes, particularly in scenarios where high temporal resolution is critical. An advantage of SRS imaging is that image acquisition rates are much higher — up to video-rate (0.1-10 s/frame) — than those achieved by spontaneous Raman spectroscopy. SRS imaging can therefore provide greater sample coverage than spontaneous Raman. A limitation of SRS microscopy, at present, is the spectral resolution, which is approximately 10 cm^{-1} for most commercial picosecond-pulsed laser-based systems. To date, many research groups have employed a dual-technique approach

for alkyne-tag Raman imaging using spontaneous Raman spectroscopy for characterising the alkyne molecule, followed by SRS imaging for biological imaging applications.

Some background and parasitic SRS signal can persist, particularly at higher laser irradiation powers (>50 mW, for example). This can result in a pump-probe process that contributes a signal that is not vibrationally dependent.[48] Several strategies for removing background signals in SRS microscopy have been developed with particular relevance to alkyne-tag SRS imaging, including the concurrent acquisition of an off-resonance image and performing a manual image subtraction, together with the use of chemometric analysis techniques to remove background and spurious signals (discussed later). In spontaneous Raman spectroscopy, a baseline fitting is routinely used for baseline correction of a sample dataset. When the baseline intensity is similar to or greater than the pure Raman spectral signal intensity, the Raman spectral peaks may be submerged or distorted due to the profile of the baseline. Therefore, a baseline correction is often applied to the raw spectrum in order to improve the accuracy of subsequent analyses. Furthermore, Raman spectral images can be acquired at a variety of different wavelengths, which can be optimized to reduce background signals such as autofluorescence. In SRS microscopy, the fluorescence signal is not problematic for imaging because of the nature of the detection of SRL and SRG at the wavelength of the pump and Stokes beams, respectively. Indeed, many groups have reported simultaneous multiphoton imaging of alkyne tagged molecules together with commercially available fluorescent stains in a multimodal imaging experiment.

In summary, spontaneous Raman and SRS imaging are well suited to biological imaging applications, particularly for ATRI. With regards to spontaneous Raman imaging, there is a clear need to increase sample imaging speeds in order to enable the technique to be competitive with faster imaging modalities. In the case of SRS imaging, the main limiting factors are the spectral resolution and the potential for background signals when the signal-to-noise of the alkyne imaging is low. There is an inherent trade-off relationship among spectral resolution, detection bandwidth, and imaging speed, making it impossible to improve all of these parameters simultaneously.

[H2] Design of alkyne-tagged compounds

Precise molecular design is crucial for ATRI. The structures and modification positions of Raman tags markedly affect detection sensitivity[3] and the size of the Raman tag must be small enough to maintain the original chemical properties of the parent molecules — particularly important when labeling small molecules. The structure–Raman shift/intensity relationship (SIR), how the chemical structure affects the Raman shift and intensity, discussed in this section forms the bedrock of these guiding principles.

[H3] Relative Raman intensity versus EdU (RIE)

The SIR of alkyne-modified molecules stored in DMSO can be determined using relative Raman intensity versus 5-ethynyl-2′-deoxyuridine (EdU) (RIE) values[3] **[G]**. Unlike the measurement of Raman intensity of sample, RIE values are calculated from the ratio of the area of alkyne peaks of EdU and sample in Raman spectra of mixture in DMSO. DMSO is widely used for stock solutions of a compound library because it can be stably stored in a solid state in the freezer and is directly applicable to biological studies, and the same solution can be applied for RIE evaluation. The RIE value, together with the detection limit of EdU by Raman microscopy, allows for the estimation of the detection limit of the alkyne or alkyne-tagged Raman probe.

When evaluating the RIE of a new compound, the reference compound can be something other than EdU, but it should possess a known RIE value and the reference peak must not overlap with the Raman signal from the compound of interes. Low-boiling-point compounds should be avoided as references due to the concentration reduction caused by evaporation on the cover glass.

A two-dimensional plot of Raman shift versus RIE of 89 alkynes — classified into 14 groups according to their substituents — is shown in FIG. 3a. These data demonstrate several general findings for improving Raman intensity of an alkyne probe and modifying their wavenumber. For example, conjugation of an aromatic ring to an alkyne results in a 5-fold increase in Raman intensity, and conjugated diynes exhibit thirteen-times-stronger intensity than their corresponding monoalkynes. Bisarylbutadiynes (BADY) stand out as the most potent category of alkyne tag, with an average RIE value of 25. Regarding the Raman shift, terminal alkynes are observed at the lower wavenumber than silyl and halo alkynes, whereas diynes and internal alkynes are observed at a higher wavenumber. These Information can help design alkyne-tagged molecules with different Raman frequencies and adequate Raman intensities allowing them to be imaged simultaneously in a multiplex imaging experiment.

[H3] Suitable modification sites for alkyne tags

Raman tags for small molecules require the smallest structure with the strongest Raman signal possible. However, in general, high-intensity tags tend to have larger structures. Using the substructure of the parent compound in the Raman tag will lead to the probes with the highest Raman intensity per structural size. For aromatic compounds, incorporating an ethynyl group conjugated with the aromatic ring (Fig. 3b) can produce Raman probes that are as sensitive as EdU, and the 1,3-butadiyne unit (diyne tag) would be suitable for aliphatic compounds showing the comparable Raman intensity to aromatic alkynes. Diyne tags can be easily prepared from terminal alkynes by cross-coupling reactions[49]. Compounds with long alkyl chains usually retain their properties, such as biological activity, even when one of the C4 unit is replaced by 1,3-

butadiyne; however, if the terminal alkyne is not available, an alternative method of synthesizing the parent compound might be required to connect the compound to the 1,3-butadiyne group. If suitable alkyl chains are not available, it is essential to explore the structure-activity relationships for modifying the molecule, considering the size and lipophilicity of the diyne tag. The bulky BADY tags is a standard tag for Raman organelle markers[50-52], sensors[6,7,53-55] and dyes[9,56], although its bulky nature means that it is not suitable for small-molecule labeling; further, its high lipophilicity often necessitates structural modifications to enhance water solubility[57].

[H3] Other Raman tags including isotopic substitution

In addition to alkynes, other functional groups such as nitriles (2200–2300 cm^{-1}), azides (~2100 cm^{-1}) and deuterium (2000-2300 cm-1) show Raman scattering in the cellular-silent region. Comparison of hexanoic acid derivatives (FIG. 3c)[2] revealed that Raman scattering of alkynes is stronger than that of nitriles. Nitriles produce stronger Raman scattering than azides, whereas C–D bonds typically produce relatively weak Raman signals with multiple peaks. The sharp and strong alkyne peak is most suitable for molecular localization analysis.

Aromatic alkynes and aliphatic alkynes are prepared through Sonogashira coupling and substitution reaction with acetylides, respectively. Substitution reactions with propargylic bromide are also applicable, using heteroatom scaffolds such as alcohols and amines. Nitriles or azides are incorporated onto aromatic rings through coupling reactions or aromatic nucleophilic substitution reactions. Additionally, alkyl nitriles and alkyl azides are synthesized through substitution reactions of cyanides and azides. However, they must be handled with caution due to the toxicity of hydrogen cyanide and the explosiveness of azides. The complex peak shape of deuterium can render deuterium labelling unsuitable for multicolor imaging. At present, the signal intensity of one deuterium is not enough for Raman imaging of bioactive compounds. However, deuterium Raman imaging has contributed to the analysis of abundant biomolecules such as lipids[58-60], sugars[61], and amino acids[62,63], which can be labeled with multiple deuterium bonds. The development of deuteration methods is currently undergoing remarkable progress and deuterated compounds are available through a wide range of deuteration reactions[64-67].

Isotopic editing **[G]** of the alkyne group is an effective strategy for modulating the vibrational frequency of the alkyne. Multicolour biomolecular detection has been demonstrated using an isotopic editing strategy based on ^{13}C labelling of the alkyne bond[68]. The differences in the reduced mass of the alkyne tag influence the stretching frequency of the alkyne group, with three fully resolved alkyne groups detected at 2125 cm^{-1} ($^{12}C{\equiv}^{12}C$), 2077 cm^{-1} ($^{13}C{\equiv}^{12}C$) and 2048 cm^{-1} ($^{13}C{\equiv}^{13}C$). This approach enabled the detection of DNA, RNA and lipids in a multiplex assay[33], and multiplex detection **[G]** of glucose metabolism was also realised using an isotopically edited

O-propargyl glucose analogue[69]. A large Raman shift of approximately 135 cm^{-1} is possible by hydrogen or deuterium exchange of terminal alkynes[70]: the Raman shift of H-alkynes (-C≡C-H) is typically in the range 2110–2120 cm^{-1}, whereas the D-alkyne (-C≡C-D) is typically in the range 1970-1985 cm^{-1}. Multicolour detection of alkynyl fatty acid probes was achieved using this method in a single-cell population. Nitrile groups have also been used with isotope editing of both carbon (^{12}C and ^{13}C) and nitrogen (^{14}N and ^{15}N) atoms[8,10,11].

[H3] Super-multiplex imaging

Approaches for modifying Raman shift or intensity such as isotope labelling accentuate the sharp features of narrow line width of Raman peaks and offers a design framework for analysing over 20 channels through super-multiplexed imaging[71]. For example, the prototype Manhattan Raman scattering (MARS) dyes feature a 24-color palette based on xanthene scaffolds modified with nitriles (FIG. 3d) [8] and an alkyne-based carbon rainbow (CARBOW) dyes, composed of 20 polyynes (FIG. 3d) has been reported[9]. Although compounds with extended repeating alkyne units require careful consideration with regards to stability (chemical stability, photostability and cellular stability), they demonstrate high sensitivity, with detection limits as low as 630 nM when using a tetrayne group. In palette design, the integration of dyes and conjugated multiple-bond structures such as alkynes or nitriles is key. The development of multi-stain palettes remains an untapped area, with future efforts likely to focus on enhancing Raman intensity and controlling intracellular localization.

[H2] Sample preparation

[H3] Cell culture/treatment for ATRI

Various cell lines have been employed for Raman imaging, including HeLa cells, MCF-7 cells, J774A.1 cells, and many other adherent and non-adherent lines. To reduce background scattered light in spontaneous Raman spectroscopy, cells are typically seeded on quartz glass or calcium fluoride of uniform thickness[15,72,73]. Cells used for SRS-based ATRI are typically seeded onto glass substrates given that fluorescence does not interfere with SRS signals. Chromophores present in the culture medium such as phenol red or those present in fetal bovine serum can interfere with Raman scattering and culture medium must be replaced with a colorless buffer solution such as Hank's balanced salt solution (HBSS) or phosphate buffered saline (PBS) immediately before measurement using Raman microscopy. Because the high concentration of DMSO interrupts the detection and affects biological homeostasis, it is important to keep the DMSO concentration as low as possible. Imaging with a 2% DMSO solution is feasible, but the background effects of DMSO should be considered at 1% or higher concentrations. If the sample contains chromophores, it should be exposed to intense light before Raman imaging to induce

fading[16,50]. Imaging with longer wavelength light (red or near-infrared light), including two-photon excitation, precludes the limitations related to background signal. In addition, SRS microscopy is compatible with multimodal imaging, in particular fluorescence microscopy.

[H3] SERS-ATRI

Nanostructured materials such as nanoparticles, roughened films or nano-patterned architectures can enhance the Raman signals of analytes through surface plasmon enhancement, by chemical contributions, or a combination of these two factors[18]. Plasmonic gold or silver nanoparticles are typically used due to their colloidal stability and large enhancement factors **[G]**, although other metals such as copper[74], aluminium[74], and magnesium[75] have been reported. Both the shape and size of nanoparticles influence the observed enhancement factor and these properties are tailored for specific applications as required[76]. Spherical, star and rod nanoparticles and nanowire have been reported, amongst other morphologies, with the morphology directly influencing the enhancement factor of the SERS effect. Spiky or pointed nanostructures generate 'hot spot' enhancement at the tip of the nanostructure but these architectures tend to be less uniform in size distribution; conversely, spheres and rods have a more even and reproducible size profile but have lower enhancement, comparatively. Larger nanoparticles generate a more intense SER signal than smaller nanoparticles, but typically have lower cell membrane permeability.

In addition, precise control of the interactions between the nanoparticles and drugs is essential. In an early study of alkyne adsorption on gold nanoparticle surfaces, both experiment and theory indicated that the magnitude of the Raman shift is highly dependent on the orientation of the alkyne bond[77,78]. The alkyne peak of phenylacetylene on gold nanoparticles was found to shift from 2111 cm^{-1} to a broad peak around 2017 cm^{-1} when phenylacetylene was installed on the surface of a gold nanoparticle, indicating the orientation of the alkyne group was perpendicular to the gold surface[77]. Similar peak broadening effects have been observed for terminal alkynes bound to silver nanoparticles[19,20]. A recent advance in SERS-ATRI was the encapsulation of alkyne-labelled compound with random orientations onto nanoparticle in a polydopamine layer, which removed the impact of molecular orientation and hence reduced the effect of peak broadening. In doing so, it enabled the creation of a super-multiplex palette of SERS nanoprobes, with each probe fine-tuned by modifying the alkyne resonance using end capping and substitution of the conjugated system[79].

[H1] Results

[H2] Data Analysis

Cellular Raman spectra are information-rich and contain a number of peaks indicative of the biomolecular content. A variety of chemometric approaches have been developed to extricate spectral features from hyperspectral imaging datasets. Generally, alkynes produce a single sharp peak in the cellular-silent region of the Raman spectrum and chemometric analysis techniques have been used to extract overlapping spectral peaks in this window (as outlined below). As another widely used bioorthogonal Raman group, deuterium labels can produce broad spectral features in the region 2000–2200 cm^{-1}. The identification of CD signals originating from different cellular biomolecules, such as lipids, proteins and DNA, can be resolved from each other using spectral unmixing and chemometric techniques[80]. Recently, the unmixing of overlapping or partially resolved alkyne and deuterium signals was reported and allowed more precise detection in the cellular-silent region in multiplexed experiments. Several chemometric techniques are described below.

[H3] Background subtraction

The Raman spectra of biological specimens often overlap with the spectral background that is attributed to autofluorescence and the extrinsic Raman scattering or fluorescence of the sample substrate, apparatus optical elements, and the sample medium. Although spectral backgrounds can be suppressed experimentally[81-88], posterior numerical processes are often necessary to subtract spectral backgrounds from measured spectra because the experimental approaches cannot fully eliminate background or have many limitations in implementation. Background arising from the sample substrate, apparatus, optical elements and sample medium are independent of the sample itself and can be subtracted by use of a reference spectrum. Reference spectra can be acquired without a biological sample[89-91] and can also be tuned to better fit the background of a measured sample by additional numerical processing such as least square approaches[91-93]. By contrast, autofluorescence contributions vary between different spectra and are therefore difficult to estimate accurately from reference spectra. The main strategy for autofluorescence subtraction is to use numerical processing, *e.g.*, iterative polynomial fitting, rolling ball algorithm, spline fitting, to estimate and subtract the broad autofluorescence contribution from an acquired spectrum[87,94-98]. Contributions from water in the specimen can also be subtracted using these numerical processes. One limitation of these numerical approaches is that the subtraction process can cause the loss of Raman signal as Raman bands can be included in the estimated broad background of acquired spectra.

[H3] Noise reduction

The Raman signals of biological specimens are often weak and can be obscured by noise. Various denoising algorithms have been developed[99], which we categorize into three groups: low-pass

filtering[100,101], curve fitting[102,103], and dimensional reduction[73,104,105]. Amongst these, low-pass filtering and curve fitting are applied to a single spectrum and remove or smooth high-frequency noise components; parameters, such as cutoff frequency in low-pass filtering and the order and window length of polynomial function in Savitzky-Golay filtering, must be adjusted for effective denoising without degrading the signal, according to spectral characteristics such as bandwidth, band shape, and signal-to-noise ratio (SNR). Low-pass filtering and curve fitting are rarely used for denoising Raman hyperspectral image datasets of biological specimens, which typically consist of a large number of spectra (≥ 10^4) containing various bands of various SNRs[15,106,107]. By contrast, dimensional reduction approaches do not require independent parameter tuning for individual spectra; this approach extracts spectral features from the whole dataset, such as hyperspectral image datasets, and reconstructs it with the spectral features that contain dominant signals.

The dimensional reduction approach, singular value decomposition[108] (SVD) has been widely used for denoising Raman hyperspectral image datasets as it does not require model tuning and initial value setting for feature extraction[15,73,106-109]. During data reconstruction, the dominant spectral features need to be properly chosen so that the noise is effectively removed while preserving major signals and avoiding artefact generation. Several algorithms have been proposed to select the most suitable singular vectors for data reconstruction[108-111].

Convolutional neural network (CNN) architectures have recently started being used for denoising Raman hyperspectral image datasets by dimensional reduction[105,112-114]. Unlike SVD, dimensional reduction by CNN is not restricted by linear decomposition of the dataset based on the data variance and in theory can give better separation of noise from signal; however, this approach requires training the model with a dataset consisting a number of low-SNR and high-SNR spectra and tuning to properly determine the architecture structure and parameters. Artifacts can be generated if the model design, tuning, and training are not properly conducted.

[H3] K-means clustering analysis

K-means clustering analysis (KMCA) is a simple, unsupervised algorithm that has been widely applied to Raman and hyperspectral SRS imaging datasets. It works by grouping spectra based on similarity (and thus, by inference, chemical composition) to identify common biochemical signatures with respective spatial distribution in imaging data sets[115]. The number of clusters (k) **[G]** is determined by the operator prior to data analysis; in doing so, each spectrum is assigned to the nearest centroid (i.e., the centre of a cluster) which are clustered based on spectral similarity. In an iterative approach, the second step is to calculate the new centroids by determining the barycentres of the clusters formed during the first round of cluster assignment. The process is cycled until convergence is reached, indicating that no movement between the

centroid positions occurs. In KMCA, the most similar spectra are clustered together and each cluster is represented by the mean spectrum of all spectra contained within it. KMCA has been used in the detection of carotenoids in B and T lymphocytes using spontaneous Raman mapping[116] and the analysis of lipid composition across a panel of prostate cancer cell models[117] and lipid metabolism in C*. elegans* worms using hyperspectral SRS[35]. KMCA has been shown to be a valuable technique for visualizing discrete regions of a sample based on composition, although visualization of data in a mean spectrum or false-color peak intensity map is susceptible to underrepresenting the subtle features contained across large spectral datasets. KMCA has been applied with other multivariate techniques such as principal component analysis (PCA) to circumvent these issues[118].

[H3] PCA and hierarchal clustering analysis

PCA is a multivariate analysis technique for spectral processing that reduces the number of variables contained within a multidimensional dataset while retaining much of the variation contained within it. The order of principal components determines their importance to describing the variance of the dataset: thus, PC1 explains the greatest variation, PC2 the second-most variation and so forth. The principal component scores are described in a loading vector plot, which in the case of Raman spectroscopy contains peaks (both positive and negative) that best explain the spectral variation across the dataset. PCA is a popular tool for the analysis of Raman spectral datasets and has been used for the determination of radiation response in glioma cell models[119] and for investigating nanoparticle treatments in cells[120]. Hierarchal clustering analysis (HCA) is another multivariate method that is often applied to Raman spectral datasets; briefly, HCA groups each spectrum in a separate cluster and iteratively groups spectra together until all are contained within a single cluster[115]. A two-dimensional dendrogram is used to show how clusters are linked, and from the dendrogram, a segmented image can be reconstructed. Unlike KMCA, there is no requirement to predefine the number of clusters in this approach.

[H3] Spectral phasor plots

Hyperspectral SRS imaging enables the characterization of a sample based on the SRS spectrum at each pixel location. Spectral phasor analysis is used to simplify complex, three-dimensional imaging SRS datasets based on x, y and λ (or cm^{-1}) coordinates. A Fourier transform is used to project the spectrum of every pixel in a 3D hyperspectral SRS image stack as a point on the 2D phasor plot, providing a global overview of the ensemble of pixels[121]. The sine and cosine components of the first term are normalized by the zero-term, resulting in a set of two

coordinates (S and G, respectively) that can be visualized in two-dimensional phasor plot. In doing so, clusters of pixels with similar spectral profiles can be segmented to identify regions of interest within the image dataset. Phasor analysis can unmix highly overlapping spectra, which is a common feature of biological Raman spectra. The separation of overlapping spectral features derived from an alkyne Raman sensor and a deuterated fatty acid in the region 2000-2250 cm^{-1} was recently enabled using spectral phasor analysis[122]. When applied to cellular imaging, the identification of nine regions of interest was shown to be possible using SPA. The approach has also been used for cellular and tissue segmentation[123,124], cytometry applications[125], exploring drug-cell interactions[126] and visualizing cellular mitosis[127].

[H2] Examples of alkyne tag Raman imaging

The key to live-cell detection of specific molecules in a Raman study is to overcome sensitivity issues. The detection limit of EdU with a high-performance Raman microscope is around 100 µM and this is a common limitation of both spontaneous Raman microscopy and SRS microscopy. Except for the use of SERS and (pre)resonance Raman scattering, observed molecules are required to be concentrated at a level greater than 100 µM (the detection limit of EdU within the cellular environment)[3]. Representative results of molecular observations are described below.

[H3] EdU

EdU is a commercially available alkyne-tagged analog of thymidine (FIG. 4a)[128]. It is covalently incorporated into replicating DNA and accumulates into the nucleus. Although imaging of EdU by fluorescent microscopy requires fixation, permeabilization, and click reaction steps for fluorescent labeling, the direct detection of EdU is possible using Raman microscopy. The characteristic alkyne peak of EdU at 2122 cm^{-1} allows for its specific detection in the presence of cellular peaks. Raman imaging of HeLa cells treated with 20 µM EdU reveals the alkyne peak of EdU localized in the nucleus (FIG. 4a)[2]. Raman imaging also provides the distribution of cellular molecules simultaneously without labeling; the merged Raman image in Fig 4a shows the distribution of cytochrome *c* (blue) and lipids (green).

[H3] Dual alkyne-tag Raman imaging

Two different alkyne-tagged compounds with distinct Raman shifts can be imaged simultaneously. AltQ2 is a short-chain ubiquinone bearing a disubstituted 1,3-butadiyne tag as a Raman tag (FIG. 4b)[3]. The alkyne peak of AltQ2 is observed at 2248 cm^{-1}, differing from the Raman shift of EdU (~2122 cm^{-1}). The spontaneous Raman imaging of HeLa cells treated with 40 µM EdU and 2 µM AltQ2 (FIG. 4b) reveals the different intracellular distributions of EdU (blue)

and AltQ2 (green). AltQ2 localizes to the cytoplasm, mitochondria (red) and lipids (not shown), while EdU localizes to the nucleus. For SRS microscopy, dual alkyne-tag imaging was performed for the first time using EdU and the alkynyl choline analogue propargylcholine (FIG. 4c)[14]. The signal of propargylcholine appeared at 2142 cm^{-1} — which is 17 cm^{-1} blueshifted relative to EdU — due to the influence of the positive charge in the alkyne vicinity.

[H1] Applications

[H2] Analysis of localization of bioactive compounds

ATRI using diynes has allowed for the observation and analysis of the intracellular distributions of small bioactive molecules that are not suitable for fluorescent labeling and imaging. For example, visualization of the structure of lipid rafts — membrane microdomains enriched in cholesterol, sphingolipids, glycolipids and saturated phospholipids — using fluorescently labelled phospholipids has proved difficult as the bulky nature of fluorophores prevents the incorporation of labelled phospholipids and causes them to localize outside the raft. This issue has been overcome using diyne-tagged sphingomyelin (diyne-SM), which can successfully integrate into lipid rafts and be visualized by Raman imaging. Diyne-SM was detected at 2262 cm^{-1} and was shown to have the original raft-forming properties of sphingomyelin (FIG. 5a)[16,129]. High-resolution ATRI revealed that diyne-SM was enriched in the central area of lipid rafts rather than in the peripheral area and distributed heterogeneously even within a single raft-mimicking domain (FIG. 5a), suggesting that the concentration of SM gradually changed to minimize the gap between SM-rich and SM-poor regions[16].

ATRI with an internal diyne has also been applied to elucidate the mode of action of coronatine (COR), a phytotoxin produced by the plant pathogen *Pseudomonas syringae*. COR has two important activities during bacterial infection through the stomata: preventing stomatal closure and inducing stomatal reopening. The former process is mediated through the plant hormone receptor COI1 and the transcriptional repressor JAZ[130], but the latter process remains unidentified. To clarify the unknown mechanism, a previous study attempted to use fluorescently labeled COR, although fluorescent labeling caused a loss of stomatal reopening activity due to the large fluorescent group (319 g/mol), which had a molecular weight comparable to that of COR [131]. A subsequent study was able to label COR using compact alkyne tags such as diynes, which enabled selective stomatal reopening activity (FIG. 5b). ATRI revealed that diyne-tagged COR in living *Arabidopsis* guard cells interacted with the second target of COR in the endoplasmic reticulum (FIG. 5b)[132]. Further biological and genetic experiments guided by

this analysis identified that the ethylene signaling pathway at the endoplasmic reticulum is involved in the stomatal reopening activity of COR [133].

SRS microscopy minimizes fluorescence interference, and SRS-ATRI can be combined with fluorescence imaging to analyze the subcellular localization of bioactive molecules using fluorescent markers (FIG. 5c). Ferrostatin-1 is a potent inhibitor of ferroptosis — a type of programmed cell death — and is known to inhibit lipid peroxidation, which is essential for ferroptosis induction. The analysis of the subcellular distribution of diyne-tagged ferrostatin by ATRI and fluorescence imaging identified the ER as the site of action of ferrostatin-1[134]. This analysis has also been applied to antimycin derivatives[135].

[H2] Quantification of drug uptake

Drug uptake can be quantified using alkyne-tagging. For example, ATRI studies of a series of diyne-tagged short-chain ubiquinones named as AltQs[3] showed that a one-carbon difference in the side chain affected the efficiency of their cellular uptake. Although the cellular uptake of ubiquinones has previously been estimated by the fractionation method[136], ATRI allows for live cell analysis without loss of compound during fractionation steps.

The combination of SERS with ATRI enables more sensitive quantification of drug uptake than ATRI alone. An alkynylated analog of the serotonin reuptake inhibitor (*S*)-citalopram (named as Alk-S-Cit) was successfully visualized in mouse brain coronal sections using SERS imaging (FIG. 6a)[26]. Silver nanoparticles were used to detect Alk-S-Cit in fixed brain sections, with alkyne peaks detected at 2118–2180 cm^{-1} (silver nanoparticles exhibit a stronger SERS signal compared to gold nanoparticles[137], but are more toxic[138]). It was observed that the Raman shift changed markedly depending on the molecular orientation of the analyte.

In living cells, the intracellular interactions of nanoparticles with specific small molecules are limited at low concentrations of drug and this principle enables digital SERS counting [139]. This technique was demonstrated in a study that monitored the uptake of the alkyne-tagged cathepsin B inhibitor Alt-AOMK using gold nanoparticles (FIG. 6b)[22]. Focusing on a single gold nanoparticle, the alkyne signal gradually appeared around 1980 cm^{-1} and then disappeared, indicating a reversible intracellular interaction between the Alt-AOMK molecule and the gold nanoparticle. A concentration-dependent increase in intracellular interactions was successfully quantified using 3D SERS imaging. In addition to drugs, Raman tags for SERS detection have been applied to quantify intracellular components such as nucleic acids, sialic acid and choline[140-142]; oxidative stress such as hydrogen peroxide[145]; and enzyme activities[146,147].

[H2] SRS imaging applied for drug analysis

The visualisation of tyrosine kinase inhibitors (TKIs) has been achieved using inherent alkyne bonds in the drug structure. An early example of this concept was demonstrated in the intracellular detection of erlotinib, which contains an inherent phenylacetylene motif that was used for detection at 2110 cm^{-1}. Erlotinib was found to be enriched in the cell periphery and the fingerprint Raman spectrum identified desmethyl erlotinib as the metabolite that is present in colon cancer cells[148]. SRS has been applied to the detection of other TKIs; for example, the spatial visualisation of ponatinib (FIG.6c) was enabled by an internal alkyne moiety that generates intense Raman scattering at 2221 cm^{-1} [149]. Using a multimodal imaging approach, the sequestration of ponatinib into lysosomes was visualised at a physiologically active treatment concentration. Given that lysosomal trapping has been proposed to reduce drug target engagement, chronic myeloid leukemia (CML) cells were pretreated with the lysosomotropic **[G]** agent choloroquine, resulting in a reduction in lysosomal accumulation of ponatinib; the inferred increase in cytosolic ponatinib enabled increased binding with its cytosolic target, BCR-ABL. A related study demonstrated the real time detection of the discoidin domain receptor 1 (DDR1) inhibitor and ponatinib structural analogue 7RH[150]. The use of a perfusion culture system enabled the long-term detection of uptake and retention in a cellular population of lung epithelial carcinoma following a 500 nM treatment concentration (FIG.6c). In each of the above studies, ATRI was used to measure the sequestration of the drug into the weakly basic environment of the lysosome and measurements were validated using multimodal imaging experiments. SRS microscopy has also been applied to drug delivery in mouse ear skin. The delivery of terbinafine, an alkyne-containing antifungal drug used to treat fungal skin infections, was shown to penetrate through the lipid-rich area, consistent with the hydrophobic nature of the drug.[14]

In the above studies, SRS imaging using an inherent alkyne tag has illuminated previously unknown aspects of drug delivery. In cases where a target molecule does not contain a bio-orthogonal Raman tag, then small alkyne tags can be an effective strategy. In one such example, the intranuclear detection of a suite of minor groove binders was realized using alkyne-tag SRS imaging[151]. A terminal alkyne tag was appended onto a known minor groove binding compound and the binding to the DNA minor groove caused red shifting of the alkyne stretching frequency, reflecting the locally hydrophobic nature of the minor groove compared to the cytoplasm.

[H2] Raman sensors for environmental changes and other reactive molecules

Raman sensors are widely used and generally detect a targeted chemical environment, for example intracellular pH, bioactive molecules or metal ions, and generate a ratiometric output based on Raman peak shifts of akyne or nitrile. Alkyne-tag Raman sensors depend on an environmental stimulus or a change in the local environment causing a structural or electronic change in close proximity to or at an alkyne reporter motif. Peak shifting in response to this change is then observed, from which a ratiometric output is provided. This is preferential because the 'before' and 'after' interaction states are stable enough to be captured under biological conditions. The BADY group has been used for sensitive detection of alkyne signal; this group generates an intense Raman scattering signal ~2220 cm^{-1} and it is possible to modulate the stretching frequency by incorporating ionisable groups in conjugation with the alkyne reporter[6]. The development of a palette of Raman sensors with pKa values in the range 2–10 has enabled pH sensing across the physiological range. Refinement of the pKa of the probe was enabled by the addition of halogen atoms onto the phenyl capping groups of the BADY structure. BADY-based pH probes have been modified for site-specific pH sensing in mitochondria through the incorporation of a triphenylphosphonium targeting group onto the BADY scaffold and by tuning the probe pKa to 7.9 using a fluorine substituent[7]. The resulting sensor, referred to as mitokyne (FIG. 7a), produced a ratiometric response for mitochondrial pH sensing during mitophagy and during inhibition of the electron transport chain and ATP synthase. The ratiometric detection of intracellular hydrogen sulfide (H_2S) was achieved by using an aromatic azide on BADY group, which is reduced to an aniline in the presence of H_2S[53]. The ratiometric output was detected as a shift from 2223 cm^{-1} to 2214 cm^{-1} and enabled the detection of NaSH, a precursor of H_2S gas in aqueous solution, at concentrations of 200 µM in cell culture. In an analogous approach, the detection of esterase activity was demonstrated by using an acetyloxymethyl ester-capped BADY probe[54]. The sensor displayed a 7.7 cm^{-1} shift (2222.8 cm^{-1} to 2215.1 cm^{-1}) upon hydrolysis of the conjugated ester group. Using this probe and spectral phasor analysis, detection of esterase activity was achieved in a single-cell population. Ratiometric sensing of ionic species has been reported, including the detection of fluoride using an alkyne sensor that yielded a 55cm^{-1} redshift upon fluoride-mediated desilylation of the alkyne group[152]. Lastly, the detection of intracellular Zn^{2+} was achieved using a phenylacetylene Raman sensor that was coupled to a dipicolylaminoethyl aniline skeleton to coordinate free Zn^{2+} [153]. The sensor generated an 8 cm^{-1} blueshift in the alkyne stretching frequency upon coordination of Zn^{2+}.

In addition to studying chemical reactions and transformations directly on the Raman probe, other studies have demonstrated that Raman peak shifts can be tuned to detect changes within the surrounding physical environment. The alkyne-containing amino acid derivatives

homopropargylglycine (HPG) and *p*-ethynylphenylalanine were introduced into the interior of the *E. coli* acyl carrier protein using a genetic code expansion technique and the Raman spectra of these derivatives indicated that alkynyl bands showed the solvatochromic shift and could act as effective probes of their local biomolecular environments [154]. In a related approach, the hydrogen-deuterium (H/D) exchange of teriminal alkyne of EdU was used to detect DNA structural changes *in situ* caused by UV damage (FIG. 7b)[155]. The formation of a UV-induced thymine dimer was observed through H/D exchange in EdU-labelled cells. By using ratiometric SRS imaging of normal EdU (SRS_H, 2224 cm^{-1}) and deuterated EdU (SRS_D, 1992 cm^{-1}), the H/D exchange in the terminal alkyne of EdU can be monitored, showing changes in the nucleus due to UV-induced thymine dimerization.

[H2] Nitrile-tag Raman imaging

Although the use of alkyne tags for Raman imaging and sensing is well established, alternative chemical functional groups that generate Raman signals in the cell-silent region of the Raman spectrum include nitriles, iso-nitriles, deuterium and carboranes have been reported[156]. Of these, the nitrile (C≡N) group has been used for both imaging and sensing purposes in a way that is analogous to the use of alkyne tags outlined in this review. For example, the nitrile group has been used as a label-free spectroscopic marker for drug localisation using both Raman and SRS microscopy. The localisation and metabolism of the tyrosine kinase inhibitor, neratinib, has been reported using the C≡N vibration at 2208 cm^{-1} in the Raman spectrum[157], and the detection of the nitrile vibration in ruxolitinib, a Janus kinase inhibitor, enabled the visualization of transdermal penetration of the drug through imaging skin using SRS microscopy at 2250 cm^{-1} [158]. The nitrile band is highly sensitive to the surrounding chemical environment and as such, several probes have been developed for ratiometric Raman sensing applications, including those for intracellular pH[159] and the ratiometric detection of biological thiols[160].

The Raman scattering cross section of the nitrile mode is typically weaker than a corresponding alkyne with a relative intensity to EdU (RIE) of ~0.06 for aliphatic nitriles, although an improvement in the RIE to ~0.48 has been reported when nitriles are conjugated to aromatic ring systems.[2] The coupling of nitrile tags to electronic pre-resonance (EPR) SRS scaffolds is an alternative means to improve the detection sensitivity of the nitrile bond. Several recent reports have described the development of nitrile-based EPR-SRS reporters for imaging and sensing purposes using the pyronine scaffold [10,161]. Isotopic editing of the CN bond using both $^{12}C/^{13}C$ and $^{14}N/^{15}N$ has also enabled multiplex detection in the EPR-SRS spectrum.

[H1] Reproducibility and data deposition

SRS microscopy has been gaining popularity, particularly for biological imaging. This is in part due to the accessibility of commercially available components for SRS imaging as most systems are home-built or custom designs. Whole SRS systems are now commercially available, which has further facilitated the transition of SRS imaging to new research communities. The intensity of the SRS signal is dependent on the effective spatiotemporal overlap of the pump and Stokes beams, and therefore any misalignment or drift will result in reduced performance. The nature of the beam path, objective and condenser lenses and detector will also impact SRS signal intensity. Given the wide variety in hardware that is available for SRS microscopy, including different laser sources (picosecond or femtosecond), excitation wavelengths and configurations of the optical components, it is perhaps unsurprising that little progress has been made in the standardisation of the technique. Most current research is aimed at exploratory development and investigation, rather than for confirmatory analysis as is routine for Raman spectroscopy in good laboratory practice (GLP) environments. Currently, the absence of standard procedures or reference materials for SRS microscopy affects the reproducibility and consistency of analysis[30]. When considering the image acquisition parameters available to be modified by the user — for example, frame size, pixel dwell time and line or frame averaging — it becomes difficult for comparisons to be drawn from images acquired on different days on the same system or from different systems on the same sample. To facilitate the transition of SRS microscopy to clinical and analytical applications in the future, the standardisation of data acquisition and data reporting is necessary.

When analysing alkyne tags, most Raman systems are calibrated to an external reference materia, such as silicon at 520.5 cm^{-1}. However, in publications using SRS imaging, it is not routine to include data on the reference material. As an emerging technique, the extent to which the reporting of image acquisition details and system parameters for imaging is variable and should be considered a priority in future studies. Discrepancies in the position of the alkyne Raman shift of EdU between labs (2118–2125 cm^{-1}) emphasises the need for standardization and reporting standards. From a practical perspective, details regarding the instrument set-up and calibration using authenticated standards represent an ideal first step. Polystyrene bead standards have been reported for super-resolution SRS microscopy and solution phase standards (including cyclohexane or ethanol, which are widely used in spontaneous Raman scattering calibration) could be a user-friendly sample type for facilitating the comparison between different SRS systems and moving towards the absolute quantification of signal intensity.

[H1] Limitations and optimisations

A main limitation in ATRI and Raman imaging in general is sensitivity. Due to the small cross-section of Raman scattering, Raman tag imaging is restricted to imaging molecules at high concentrations. Concentrations of approximately 100 μM are the lowest that both spontaneous Raman and SRS microscopy can readily detect for mono-alkynes and diynes. Although SRS can amplify Raman signals, the intrinsic background of cross-phase modulation and laser shot noise also increase, resulting in the sensitivity of SRS microscopy in detecting low concentration molecules being comparable to that of spontaneous Raman microscopy[162]. In Raman microscopy, the presence of fluorescence in the sample considerably diminishes sensitivity in detecting Raman peaks. SERS can be used to amplify the Raman signal, although signal enhancement is heavily reliant on the local structure of the metal used and its surface condition, and it is therefore challenging to use SERS for the quantitative measurement of molecules. However, the digital counting of SERS spots can be used to assess relative concentrations under different conditions[22] or even quantify low-concentration molecules when single-molecule detection sensitivity is achieved[139,163,164].

Because of the low sensitivity of Raman, laser power and exposure time must be carefully optimized to avoid optical damage to the sample. Time-lapse imaging is especially susceptible to issues with photodamage. It is always advisable to check cell viability with respect to the exposure conditions used in the experiment. Photodamage also depends on the excitation wavelength; the use of longer wavelengths will result in less photodamage but will cause a decrease in Raman signal intensity and sensitivity. SERS can mitigate this limitation as specially designed SERS probes enable the use of red to near-infrared (NIR) wavelengths to enhance signal[165,166]. As photodamage can occur nonlinearly with respect to excitation intensity, reducing the excitation power while increasing exposure time can be beneficial. Additionally, lowering the sample temperature reduces photodamage, particularly that associated with resonant Raman scattering[167]. Reducing the image resolution (scanning pitch) also reduces total exposure to the sample and reducing the spatial and spectral resolution can reduce noise and increase sensitivity in detection processes such as signal amplification and readout. These conditions should be selected according to the sample and purpose, which is always a key factor for successful ATRI.

[H1] Outlook

In this Primer, we summarized basic concepts, experimental procedures and applications of ATRI and alkyne-tag Raman sensing, and how these methods can be used as an alternative to fluorescent imaging and probes. The combination of alkyne-tags and Raman imaging can be used to visualize the cellular uptake and distribution of small bioactive compounds that aredifficult to label with fluorescent tags, and it is expected to contribute to the mechanistic study of bioactive

compounds and drug development[168]. Although the low sensitivity of Raman imaging limits the application of alkyne tags, new technologies to improve detection sensitivity would realize the broad application of ATRI as a standard analysis tool for bioactive compounds. In addition to alkynes, other tags such as nitriles and deuterium labelling are also suitable for Raman imaging and should broaden the applications of Raman tags in future. With improved sensitivity, deuterium might be most useful for Raman imaging of drug candidates; compared with alkyne tags, deuterium tags have very weak Raman signal but with the less perturbation on bioactivity than alkyne tag and maintain the original chemical structure of the target compound, making them ideal for drug imaging. Furthermore, during drug development, deuterated derivatives are often developed and used for metabolic analysis[169] and deuterated drug candidates could therefore be applied for Raman imaging.

Various fluorescent probes have been developed and widely used to detect biological signals, and Raman probes could also be applied for these studies. Further, the high wavenumber resolution of Raman probes makes them suitable for super-multiplex imaging[13,14,170]. Raman dots and polymeric nanoparticles encapsulating Raman dyes have been developed for the labeling of antibodies, which can be used for immunostaining[56] in an approach similar to quantum dots. Photoactivatable Raman probes have also been reported for pulse-chase imaging of cellular organelles[171]. Recently developed photo-switchable Raman probes have enabled super-resolution Raman imaging[172,173] and several strategies for super-resolution SRS imaging have been reported[174]. These recent reports demonstrate the potential of Raman imaging, with the creation of Raman probes that are comparable to conventional fluorescent reporters with a miniaturized design. In addition to Raman microscopy, other Raman detection systems, such as Raman-based cell sorting systems[175] and Raman plate readers[176], are also expected to be used for ATRI in the future. Indeed, a Raman plate reader has already been applied for the screening of drug polymorphisms and alkyne-labeled proteins and peptides[176]. Alkyne tag Raman imaging and sensing has opened new applications of Raman imaging in biological research, especially in chemical biology research. We expect further applications of Raman imaging and probes to lead to innovative findings and methods in the life sciences.

Author contributions

Introduction (K.D. and M.S.); Experimentation (H.Y., W.J.T. and T.K.); Results (W.J.T., H.Y. and Y.K.); Applications (W.J.T., S.E. and H.Y.); Reproducibility and data deposition (W.J.T., K. Faulds, and D.G.); Limitations and optimizations (Y.K. and K.Fujita); Outlook (K.D. and M.S.); Overview of the Primer (K.D., D.G., K.Fujita and M.S.).

Competing interests

The authors declare no competing interests.

Figures

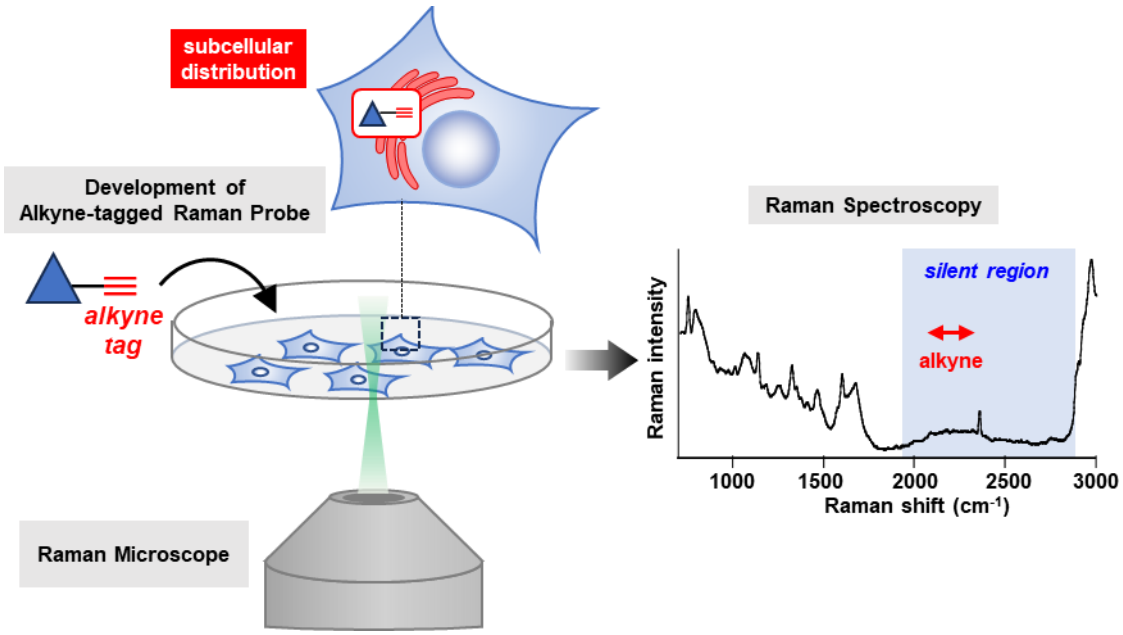

Fig. 1 **Summary of Alkyne-tag Raman Imaging.**

Alkyne tags are small functional groups that produce a strong Raman signal in cellular-silent region (a region of the Raman spectrum where endogenous molecules show no strong Raman peaks). Labelling a target compound with an alkyne tag allows the compound to be visualized intracellularly using Raman imaging to determine its subcellular location.

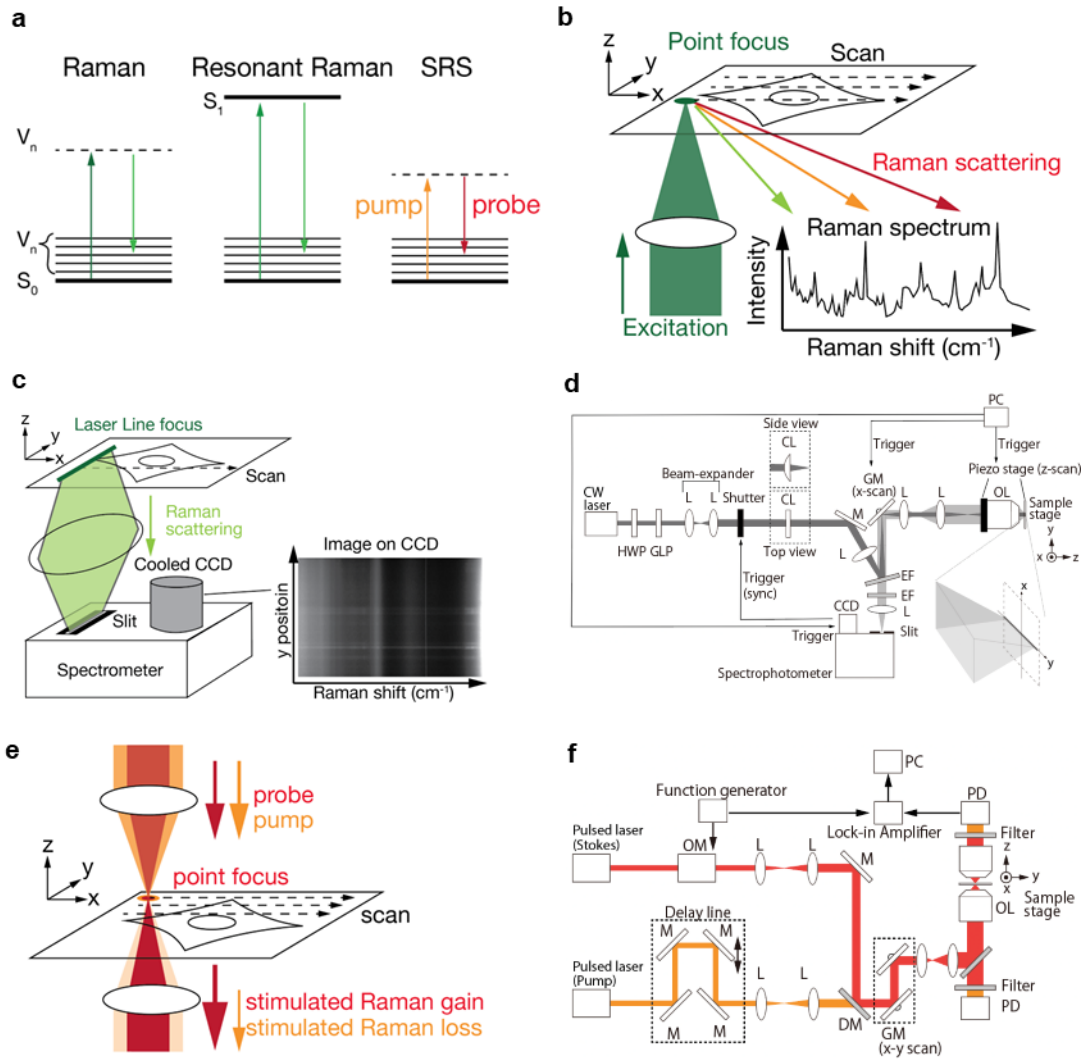

Fig. 2 **Setup of the Raman microscope.** A, Energy level diagram of Raman scattering, resonant Raman scattering, and stimulated Raman scattering (SRS). S_0, S_1, and V_n represent the electric ground state, electric first excited state, and the vibrational excited states, respectively. B, Basic principle of spontaneous Raman microscopy. The laser beam is scanned over a region of interest to generate a hyperspectral Raman image. C, Basic principle of a slit-scanning confocal spontaneous Raman microscope. The excitation light is focused in a line-shape onto samples and the spectra of the induced Raman scattering are simultaneously imaged using a 2D image sensor, resulting in faster imaging. D, Optical setup of a slit-scanning spontaneous Raman microscope. A high-power CW laser is employed for the excitation light source; the combination of a HWP and a GLP enables control the power of excitation laser. A beam expander then collimates and expands the laser beam. A CL shapes the excitation beam into a line-shaped focus and the excitation light is projected onto the sample position by an OL. The Raman scattered light, collected by the same OL, is separated from the

laser beam by a set of long-pass EFs and imaged on a confocal slit at the entrance of a spectrophotometer. The Raman scattered light is dispersed by a grating in the spectrophotometer and imaged on a 2D image sensor. Cooled CCD cameras or electron-multiplying CCD cameras are typically used for Raman and SERS measurements, respectively. The laser focus is scanned over the sample by a GM or a piezo stage anti-synchronized with the CCD exposure. To prevent light exposure to the CCD pixels during readout, the shutter is synchronized and closed at the CCD exposure. An excitation wavelength is typically selected from 532–785 nm, considering the amount of Raman scattering, including resonance effect, autofluorescence, and photodamage. The grating density is selected considering the required spectral resolution. E, Basic principle of SRS microscopy. Two ultrashort-pulse lasers serve as the pump and Stokes beam and are focused on the sample. When the molecular vibrational energy matches the wavelength difference between the pump and Stokes beams, it is selectively detected as stimulated Raman loss and stimulated Raman gain due to the energy exchange between the two beams. F, Optical setup of a SRS microscope. Two pulsed lasers are used for the pump and Stokes beams, with wavelengths in the range of 1000–1100 nm and 750–1100 nm, respectively. The pulse width is typically in the order of picoseconds to match the molecular vibration bandwidth. High laser repetition rates (>1MHz) are preferred to suppress low-frequency noise due to laser fluctuations. An OM is inserted into one of the beam paths. An AOM or EOM is typically used; although either an AOM or EOM is sufficient for SRS imaging, the EOM is capable of faster modulation. A delay-line is inserted in one of the beam paths to adjust the temporal overlap of the beams and the divergence of the laser beams is adjusted by beam expanders. A DM with an edge wavelength in between that of the Stokes and Pump beams is inserted to combine the two laser beams. The paths of the two beams are aligned so that they are focused on the same position of the sample by an OL with temporal overlap. The laser beams transmitted through the sample are collected by a condenser lens and the pump beam is selectively detected by an optical filter and a . The detected signal is demodulated by a lock-in amplifier with the SRL or SRG signal detected at the modulation frequency applied to the Stokes beam. AOM, acousto-optical modulator; CL, cylindrical lens; CW, continuous wave; DM, dichroic mirror; EF, edge filter; EOM, electro-optical modulator; HWP, half-wave plate **[G]**; GLP, glan laser prism; OM, optical modulator **[G]**; L, lens; M, mirror; GM, Galvanometric mirror; OL, objective lens; PD, photo detector.

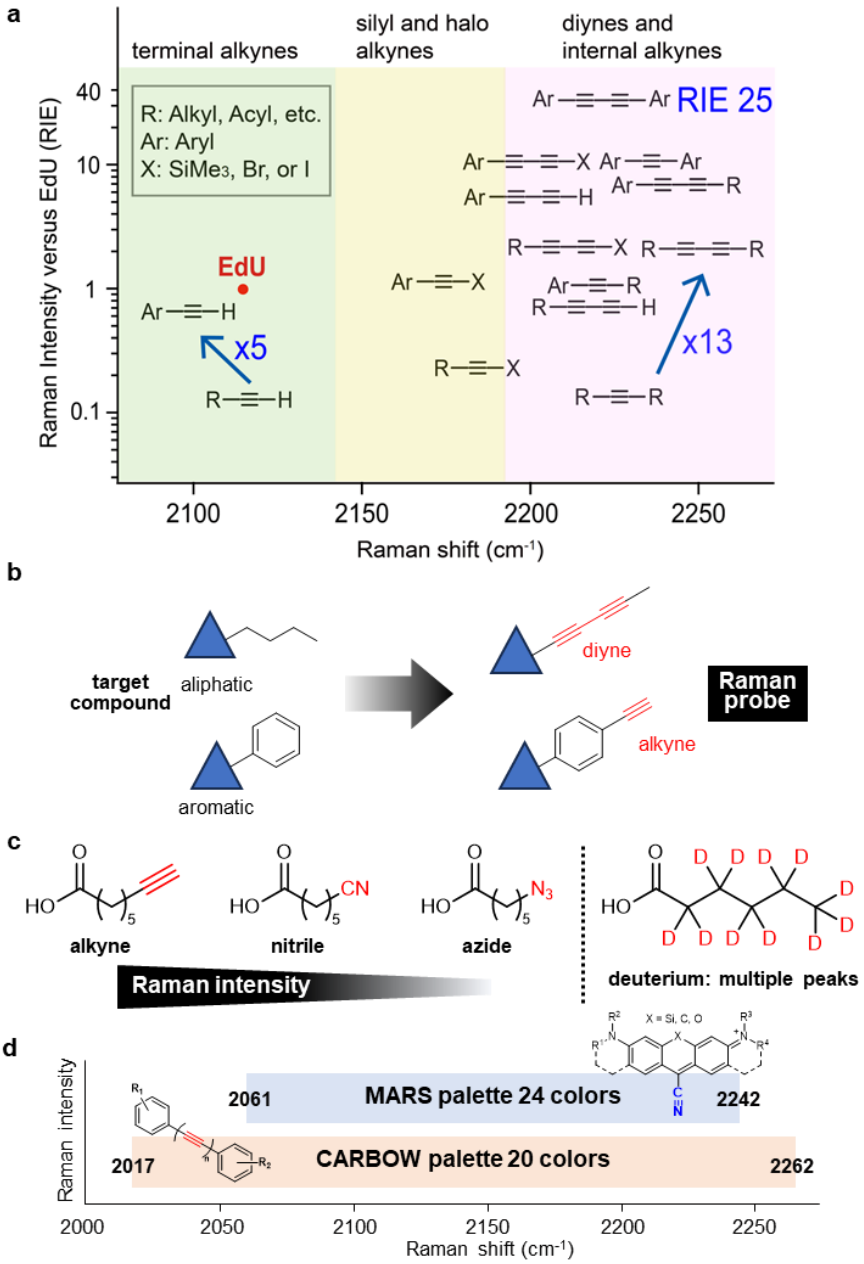

Fig. 3 **Development of Alkyne-tagged Raman Probes.** A, Relative Raman intensities versus EdU (RIE) and Raman shifts plotted for various types of alkynes, quantified in comparison with EdU (red dot). In the evaluation of terminal alkynes, benzonitrile was used as a control compound due to their overlapping peaks with EdU. B, Design principles of an alkyne-tagged Raman probe detectable by Raman imaging. For aromatic compounds, a terminal alkyne conjugated with aromatic ring is suitable. For aliphatic compounds, a diyne tag is suitable. C, Comparison of Raman intensities of various tags, including alkynes, nitriles, azides and deuterium. D, Color palettes for super-multiplexed imaging. MARS dye, Manhattan Raman scattering dye; CARBOW dye, carbon rainbow dye.

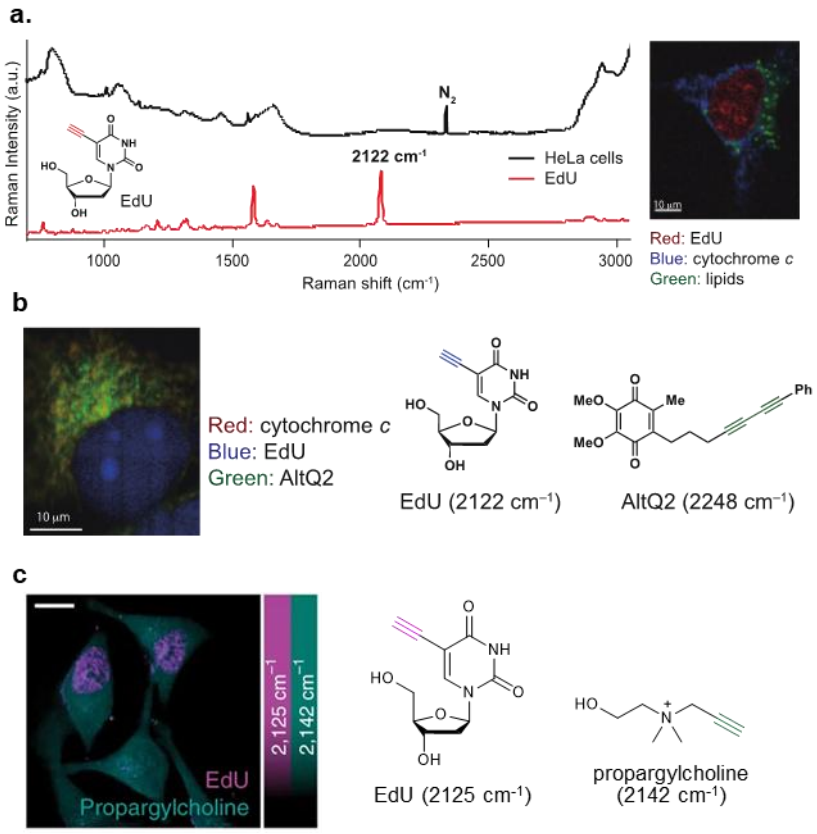

Fig. 4 **Alkyne-tag Raman imaging in live cells**

a. Raman spectra of EdU and HeLa cells. HeLa cells were treated with 20 μM EdU for 6 h, and observed by Raman microscopy (excitation at 532 nm). Merged image was obtained from Raman images at 749 cm^{-1} (blue, cytochrome c), 2123 cm^{-1} (red, EdU), and 2849 cm^{-1} (green, lipid). The signal derived from alkyne tag of EdU was observed in the nucleus. Adapted with permission from REF.[2], ACS. B, Dual alkyne-tag Raman Imaging of HeLa cells treated with EdU (blue, 2122 cm^{-1}) and AltQ2 (green, 2248 cm^{-1}). Two different compounds can be visualized simultaneously. Adapted with permission from REF.[3], ACS. C, SRS imaging of HeLa cells treated with EdU (magenta, 2125 cm^{-1}) and propargylcholine (green, 2142 cm^{-1}). Alkyne-tag Raman imaging was successfully applied for SRS imaging. Adapted with permission from REF.[14], Springer Nature. Scale bars, 10 μm.

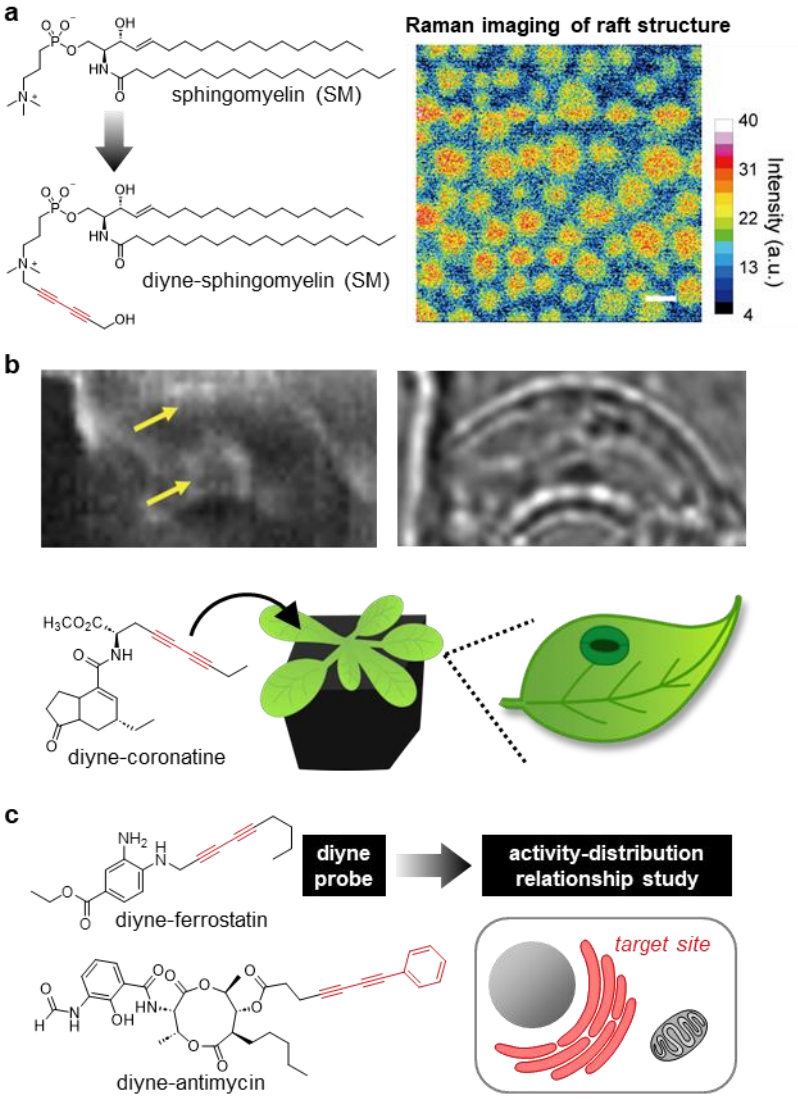

Fig. 5 **Application of diyne probes for biological studies**

a. Diyne-tagged sphingomyelin (diyne-SM) was developed and visualized by Raman imaging in raft-mimicking domains on a quartz substrate. Raft mimicking domains were formed in diyne-SM/dioleoyl-phosphatidylcholine (DOPC)/cholesterol ternary monolayers (1/1/1 molar ratio) showing phase segregation property. Adapted from REF.[17] b, Raman imaging of living guard cells treated with 100 µM diyne-tagged coronatine (diyne-COR) for 3 h in isolated leaf epidermis of *Arabidopsis thaliana*. Diyne-COR is localized primarily in the perinuclear region, including ER, as indicated by the yellow arrows. Adapted with permission from REF.[126], ACS. c, Mechanistic studies of diyne-tagged bioactive compounds. The cellular distribution of diyne-tagged bioactive compounds was analyzed by SRS microscopy and compared with fluorescent organelle markers to identify their sites of action.

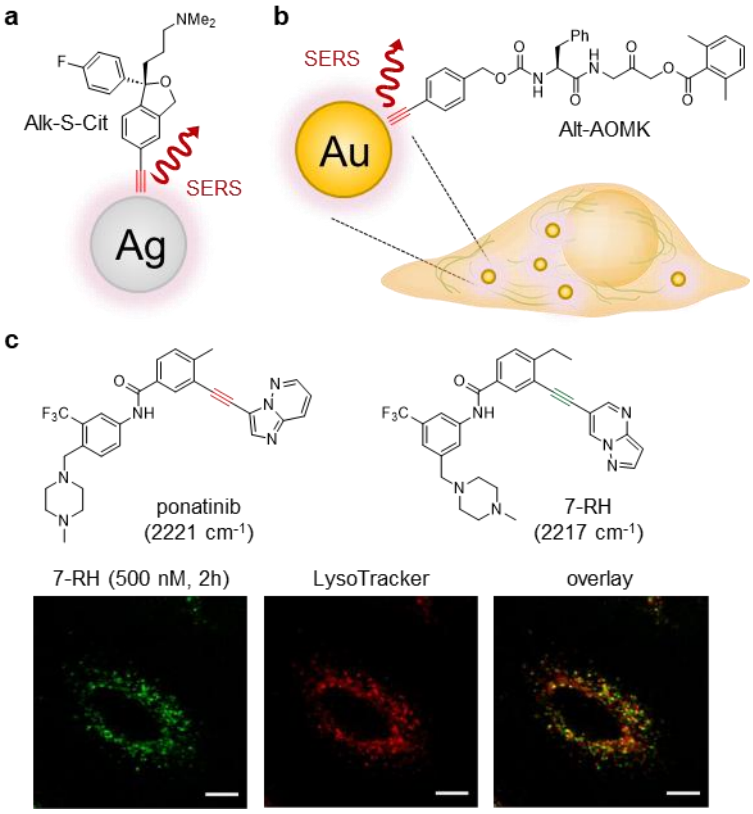

Fig. 6 **Quantification of drug uptake**

a. SERS signal obtained from the interaction between silver nanoparticles and alkyne-tagged (*S*)-citalopram (Alk-S-Cit). B, SERS signal obtained from the interaction between gold nanoparticles and an alkyne-tagged cathepsin B inhibitor Alt-AOMK. By using 3D-SERS imaging, uptake of Alt-AOMK was quantified. C, Cellular uptake of a kinase inhibitor 7-RH, a derivative of ponatinib, was quantified by using SRS imaging. Overlay image was obtained from Raman image at 2217 cm^{-1} (green, alkyne of 7-RH) and a fluorescent image (Lysotracker red, excitation 561 nm/emission 565-650 nm). Lysosomal accumulation of 7-RH can be quantified by combination with SRS imaging and fluorescent imaging. Adapted with permission from REF.[144], the Royal Society of Chemistry. Scale bars, 10 µm.

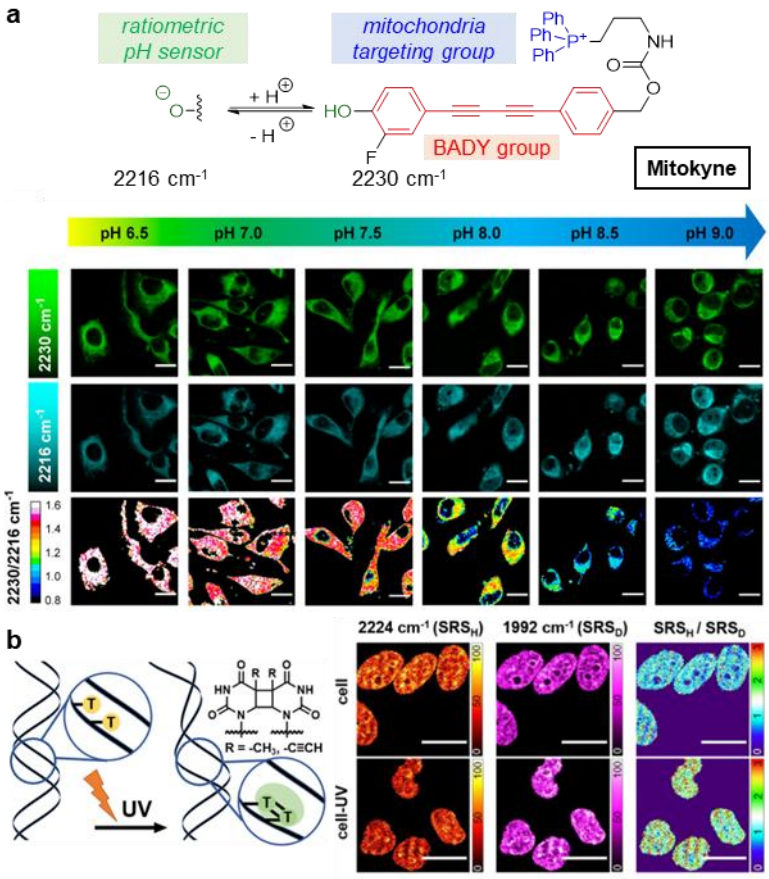

Fig. 7 **Alkyne-tagged Raman sensors**

a. Mitokyne, a mitochondria-specific pH sensor. HeLa cells were treated with Mitokyne under different pH conditions. SRS images at 2230 and 2216 cm^{-1} can be used to quantify the pH values. Adapted with permission from REF.[7], ACS. B, Monitoring UV-induced DNA damage in EdU-labeled HeLa cells within DPBS-D_2O buffer using SRS microscopy. Ratiometric SRS imaging of normal EdU (SRS_H, 2224 cm^{-1}) and deuterated EdU (SRS_D, 1992 cm^{-1}) enables the observation of H/D exchange in the terminal alkyne of EdU, reflecting environmental changes in the nucleus caused by UV-induced thymine dimerization. Adapted with permission from REF.[149], ACS.

Table 1. Comparison of spontaneous Raman and SRS microscopy. Typical values are displayed and vary up to options of the optics.

Technique	**Spatial resolution (μm)**	**Spectral resolution (cm^{-1})**	**Spectral detection bandwidth (cm^{-1})**	**Imaging speed**	**Fluorescent background**	**Suitable applications**
Spontaneous Raman imaging (line illumination)	0.3 (XY), 1 (Z)	0.1 to 10	3000	>10 min/frame	Strongly affected	Spectral analysis of compound Simultaneous imaging of intrinsic biomolecules and alkyne-tagged molecules Combination with SERS imaging Ratiometric Raman sensor Fixed sample
SRS imaging	0.3 (XY), 1-2 (Z)	~1 to 50	~10 to 1000	0.1-10 s/frame	No effect	Video-rate imaging Multicolor imaging of alkyne-tagged molecules Multimodal imaging with fluorescent staining

Reference

1. Raman, C. V. & Krishnan, K. S. The Negative Absorption of Radiation. *Nature* **122**, 12–13 (1928).

   The first description of Raman scattering.

2. Yamakoshi, H. *et al.* Imaging of EdU, an Alkyne-Tagged Cell Proliferation Probe, by Raman Microscopy. *J. Am. Chem. Soc.* **133**, 6102–6105 (2011).

   This article is the first conceptual demonstration of alkyne-tag Raman imaging (ATRI).

3. Yamakoshi, H. *et al.* Alkyne-tag Raman imaging for visualization of mobile small molecules in live cells. *J. Am. Chem. Soc.* **134**, 20681–9 (2012).

   This article provides the structure-Raman shift/intensity relationship of alkynes and is the first conceptual demonstration of dual ATRI.

4. Bakthavatsalam, S., Dodo, K. & Sodeoka, M. A decade of alkyne-Tag Raman imaging (ATRI): Applications in biological systems. *RSC Chem. Biol.* **2**, 1415–1429 (2021).
5. Dodo, K., Fujita, K. & Sodeoka, M. Raman Spectroscopy for Chemical Biology Research. *J. Am. Chem. Soc.* **144**, 19651–19667 (2022).
6. Wilson, L. T. *et al.* A new class of ratiometric small molecule intracellular pH sensors for Raman microscopy. *Analyst* **145**, 5289–5298 (2020).
7. Wilson, L. T. *et al.* Mitokyne: A Ratiometric Raman Probe for Mitochondrial pH. *Anal. Chem.* **93**, 12786–12792 (2021).
8. Wei, L. *et al.* Super-multiplex vibrational imaging. *Nature* **544**, 465–470 (2017).

   This article is the first conceptual demonstration of super-multiplex imaging of Manhattan Raman Scattering (MARS) dyes via electronic pre-resonance SRS.

9. Hu, F. *et al.* Supermultiplexed optical imaging and barcoding with engineered polyynes. *Nat. Methods* **15**, 194–200 (2018).
10. Fujioka, H. *et al.* Multicolor Activatable Raman Probes for Simultaneous Detection of Plural Enzyme Activities. *J. Am. Chem. Soc.* **142**, 20701–20707 (2020).

    This article is the first conceptual demonstration of Raman sensors for enzyme activities.

11. Fujioka, H. *et al.* Activatable Raman Probes Utilizing Enzyme-Induced Aggregate Formation for Selective Ex Vivo Imaging. *J. Am. Chem. Soc.* **145**, 8871–8881 (2023).
12. Min, W., Freudiger, C. W., Lu, S. & Xie, X. S. Coherent nonlinear optical imaging: beyond fluorescence microscopy. *Annu. Rev. Phys. Chem.* **62**, 507–30 (2011).
13. Freudiger, C. W. *et al.* Label-Free Biomedical Imaging with High Sensitivity by Stimulated Raman Scattering Microscopy. *Science* **322**, 1857–1861 (2008).

This article is the first conceptual demonstration of SRS imaging of intracellular biomolecules.

14. Wei, L. *et al.* Live-cell imaging of alkyne-tagged small biomolecules by stimulated Raman scattering. *Nat. Methods* **11**, 410–412 (2014).

This article is the first conceptual demonstration of ATRI using SRS microscopy.

15. Palonpon, A. F. *et al.* Raman and SERS microscopy for molecular imaging of live cells. *Nat. Protoc.* **8**, 677–92 (2013).
16. Ando, J. *et al.* Sphingomyelin distribution in lipid rafts of artificial monolayer membranes visualized by Raman microscopy. *Proc. Natl. Acad. Sci. U. S. A.* **112**, 4558–4563 (2015).
17. Efremov, E. V., Ariese, F. & Gooijer, C. Achievements in resonance Raman spectroscopy review of a technique with a distinct analytical chemistry potential. *Anal. Chim. Acta* **606**, 119–34 (2008).
18. Han, X.X., Rodriguez, R.S., Haynes, C.L. *et al.* Surface-enhanced Raman spectroscopy. *Nat. Rev. Methods Primers* **1**, 87 (2021).
19. Kennedy, D. C., McKay, C. S., Tay, L. L., Rouleau, Y. & Pezacki, J. P. Carbon-bonded silver nanoparticles: Alkyne-functionalized ligands for SERS imaging of mammalian cells. *Chem. Commun.* **47**, 3156–3158 (2011).

This article is the first conceptual demonstration of SERS-ATRI.

20. Ando, J. *et al.* Alkyne-tag SERS screening and identification of small-molecule-binding sites in protein. *J. Am. Chem. Soc.* **138**, 13901–13910 (2016).
21. Li, M. *et al.* Alkyne-and nitrile-anchored gold nanoparticles for multiplex SERS imaging of biomarkers in cancer cells and tissues. *Nanotheranostics* **3**, 113–119 (2019).
22. Koike, K. *et al.* Quantitative Drug Dynamics Visualized by Alkyne-Tagged Plasmonic-Enhanced Raman Microscopy. *ACS Nano* **14**, 15032–15041 (2020).

23. Zhang, S., Mei, Y., Liu, J., Liu, Z. & Tian, Y. Alkyne-tagged SERS nanoprobe for understanding Cu+ and Cu2+ conversion in cuproptosis processes. *Nat. Commun.* **15**, 3246 (2024).
24. Ando, J., Fujita, K., Smith, N. I. & Kawata, S. Dynamic SERS imaging of cellular transport pathways with endocytosed gold nanoparticles. *Nano Lett.* **11**, 5344–5348 (2011).
25. Ardini, M. *et al.* Live Intracellular Biorthogonal Imaging by Surface Enhanced Raman Spectroscopy using Alkyne-Silver Nanoparticles Clusters. *Sci. Rep.* **8**, 12652 (2018).
26. Tanuma, M. *et al.* Direct visualization of an antidepressant analog using surface-enhanced Raman scattering in the brain. *JCI Insight* **5**, e133348 (2020).
27. Tsikritsis, D., Legge, E. J. & Belsey, N. A. Practical considerations for quantitative and reproducible measurements with stimulated Raman scattering microscopy. *Analyst* **147**, 4642–4656 (2022).
28. Li, Y. *et al.* Review of Stimulated Raman Scattering Microscopy Techniques and Applications in the Biosciences. *Adv. Biol.* **5**, e2000184 (2021).
29. Hu, F., Shi, L. & Min, W. Biological imaging of chemical bonds by stimulated Raman scattering microscopy. *Nat. Methods* **16**, 830–842 (2019).
30. Freudiger, C. W. *et al.* Highly specific label-free molecular imaging with spectrally tailored excitation-stimulated Raman scattering (STE-SRS) microscopy. *Nat. Photonics* **5**, 103–109 (2011).
31. Suhalim, J. L. *et al.* Characterization of cholesterol crystals in atherosclerotic plaques using stimulated Raman scattering and second-harmonic generation microscopy. *Biophys. J.* **102**, 1988–1995 (2012).
32. Kong, L. *et al.* Multicolor stimulated Raman scattering microscopy with a rapidly tunable optical parametric oscillator. *Opt. Lett.* **38**, 145–147 (2013).
33. Wang, P. *et al.* Label-Free Quantitative Imaging of Cholesterol in Intact Tissues by Hyperspectral Stimulated Raman Scattering Microscopy. *Angew. Chemie Int. Ed.* **52**, 13042–13046 (2013).
34. Zhang, D. *et al.* Quantitative vibrational imaging by hyperspectral stimulated Raman scattering microscopy and multivariate curve resolution analysis. *Anal. Chem.* **85**, 98–106 (2013).
35. Wang, P. *et al.* Imaging Lipid Metabolism in Live Caenorhabditis elegans Using Fingerprint Vibrations. *Angew. Chemie Int. Ed.* **53**, 11787–11792 (2014).
36. Andresen, E. R., Berto, P. & Rigneault, H. Stimulated Raman scattering microscopy by spectral focusing and fiber-generated soliton as Stokes pulse. *Opt. Lett.* **36**, 2387–2389 (2011).

37. Fu, D., Holtom, G., Freudiger, C., Zhang, X. & Xie, X. S. Hyperspectral Imaging with Stimulated Raman Scattering by Chirped Femtosecond Lasers. *J. Phys. Chem. B* **117**, 4634–4640 (2013).
38. He, R. *et al.* Stimulated Raman scattering microscopy and spectroscopy with a rapid scanning optical delay line. *Opt. Lett.* **42**, 659–662 (2017).
39. Alshaykh, M. S. *et al.* High-speed stimulated hyperspectral Raman imaging using rapid acousto-optic delay lines. *Opt. Lett.* **42**, 1548–1551 (2017).
40. Liao, C.-S. *et al.* Stimulated Raman spectroscopic imaging by microsecond delay-line tuning. *Optica* **3**, 1377–1380 (2016).
41. Lu, F.-K. *et al.* Multicolor stimulated Raman scattering (SRS) microscopy. *Mol. Phys.* **110**, 1927–1932 (2012).
42. Seto, K., Okuda, Y., Tokunaga, E. & Kobayashi, T. Development of a multiplex stimulated Raman microscope for spectral imaging through multi-channel lock-in detection. *Rev. Sci. Instrum.* **84**, 083705 (2013).
43. Rock, W., Bonn, M. & Parekh, S. H. Near shot-noise limited hyperspectral stimulated Raman scattering spectroscopy using low energy lasers and a fast CMOS array. *Opt. Express* **21**, 15113–15120 (2013).
44. Liao, C.-S. *et al.* Microsecond Scale Vibrational Spectroscopic Imaging by Multiplex Stimulated Raman Scattering Microscopy. *Light. Sci. Appl.* **4**, e265 (2015).
45. Fu, D. *et al.* Quantitative chemical imaging with multiplex stimulated Raman scattering microscopy. *J. Am. Chem. Soc.* **134**, 3623–3626 (2012).
46. Liao, C.-S. *et al.* Spectrometer-free vibrational imaging by retrieving stimulated Raman signal from highly scattered photons. *Sci. Adv.* **1**, e1500738 (2015).
47. Saltarelli, F. *et al.* Broadband stimulated Raman scattering spectroscopy by a photonic time stretcher. *Opt. Express* **24**, 21264–21275 (2016).
48. Zhang, D., Wang, P., Slipchenko, M. N. & Cheng, J.-X. Fast vibrational imaging of single cells and tissues by stimulated Raman scattering microscopy. *Acc. Chem. Res.* **47**, 2282–90 (2014).
49. Yin, W., He, C., Chen, M., Zhang, H. & Lei, A. Nickel-catalyzed oxidative coupling reactions of two different terminal alkynes using O_2 as the oxidant at room temperature: facile syntheses of unsymmetric 1,3-diynes. *Org. Lett.* **11**, 709–12 (2009).
50. Yamakoshi, H. *et al.* A sensitive and specific Raman probe based on bisarylbutadiyne for live cell imaging of mitochondria. *Bioorganic Med. Chem. Lett.* **25**, 664–667 (2015).
51. Bae, K., Zheng, W., Ma, Y. & Huang, Z. Real-time monitoring of pharmacokinetics of mitochondria-targeting molecules in live cells with bioorthogonal hyperspectral stimulated Raman scattering microscopy. *Anal. Chem.* **92**, 740–748 (2020).

52. Ding, C. *et al.* Photostable lysosomal imaging of living cell with hyperspectral stimulated Raman scattering microscopy using a probe based on bisarylbutadiyne. *Chinese Chem. Lett.* **30**, 1393–1396 (2019).
53. Zeng, C., Hu, F., Long, R. & Min, W. A ratiometric Raman probe for live-cell imaging of hydrogen sulfide in mitochondria by stimulated Raman scattering. *Analyst* **143**, 4844–4848 (2018).

This article is the first conceptual demonstration of Raman sensors for intracellular reactive molecules.

54. Braddick, H. J. *et al.* Determination of Intracellular Esterase Activity Using Ratiometric Raman Sensing and Spectral Phasor Analysis. *Anal. Chem.* **95**, 5369–5376 (2023).
55. Ravindra, M. P. *et al.* Stretching the Bisalkyne Raman Spectral Palette Reveals a New Electrophilic Covalent Motif. *Chem. Eur. J.* **29**, e202300953 (2023).
56. Zhao, Z. *et al.* Ultra-bright Raman dots for multiplexed optical imaging. *Nat. Commun.* **12**, 1305 (2021).
57. Kawaguchi, M. *et al.* Visualization of Modified Bisarylbutadiyne-Tagged Small Molecules in Live-Cell Nuclei by Stimulated Raman Scattering Microscopy. *Anal. Chem.* **96**, 6643–6651 (2024).
58. Fu, D. *et al.* In vivo metabolic fingerprinting of neutral lipids with hyperspectral stimulated Raman scattering microscopy. *J. Am. Chem. Soc.* **136**, 8820–8828 (2014).
59. Dodo, K. *et al.* Synthesis of deuterated γ-linolenic acid and application for biological studies: metabolic tuning and Raman imaging. *Chem. Commun.* **57**, 2180–2183 (2021).
60. Egoshi, S., Dodo, K. & Sodeoka, M. Deuterium Raman imaging for lipid analysis. *Curr. Opin. Chem. Biol.* **70**, 102181 (2022).
61. Zhang, L. *et al.* Spectral tracing of deuterium for imaging glucose metabolism. *Nat. Biomed. Eng.* **3**, 402–413 (2019).
62. Miao, K. & Wei, L. Live-Cell Imaging and Quantification of PolyQ Aggregates by Stimulated Raman Scattering of Selective Deuterium Labeling. *ACS Cent. Sci.* **6**, 478–486 (2020).
63. Spratt, S. J. *et al.* Probing Methionine Uptake in Live Cells by Deuterium Labeling and Stimulated Raman Scattering. *J. Phys. Chem. B* **126**, 1633–1639 (2022).
64. Ranjan, P., Pillitteri, S., Van der Eycken, E. V. & Sharma, U. K. Photochemical methods for deuterium labelling of organic molecules. *Green Chem.* **22**, 7725–7736 (2020).
65. Kopf, S. *et al.* Recent Developments for the Deuterium and Tritium Labeling of Organic Molecules. *Chem. Rev.* **122**, 6634–6718 (2022).
66. Li, N., Li, Y., Wu, X., Zhu, C. & Xie, J. Radical deuteration. *Chem. Soc. Rev.* **51**, 6291–6306 (2022).

67. Moriyama, S. *et al.* Multiple deuteration of triphenylphosphine and live-cell Raman imaging of deuterium-incorporated Mito-Q. *Chem. Commun.* **59**, 12100–12103 (2023).
68. Chen, Z. *et al.* Multicolor live-cell chemical imaging by isotopically edited alkyne vibrational palette. *J. Am. Chem. Soc.* **136**, 8027–8033 (2014).

This article is the first conceptual demonstration of three-color ATRI of isotopic alkynes.

69. Long, R. *et al.* Two-color vibrational imaging of glucose metabolism using stimulated Raman scattering. *Chem. Commun.* **54**, 152–155 (2018).
70. Egoshi, S., Dodo, K., Ohgane, K. & Sodeoka, M. Deuteration of terminal alkynes realizes simultaneous live cell Raman imaging of similar alkyne-tagged biomolecules. *Org. Biomol. Chem.* **19**, 8232–8236 (2021).
71. Du, J., Wang, H. & Wei, L. Bringing Vibrational Imaging to Chemical Biology with Molecular Probes. *ACS Chem. Biol.* **17**, 1621–1637 (2022).
72. Kann, B., Offerhaus, H. L., Windbergs, M. & Otto, C. Raman microscopy for cellular investigations--From single cell imaging to drug carrier uptake visualization. *Adv. Drug Deliv. Rev.* **89**, 71–90 (2015).
73. Uzunbajakava, N. *et al.* Nonresonant Raman imaging of protein distribution in single human cells. *Biopolymers* **72**, 1–9 (2003).
74. Rodriguez, R. D. *et al.* Aluminum and copper nanostructures for surface-enhanced Raman spectroscopy: A one-to-one comparison to silver and gold. *Sensors Actuators, B Chem.* **262**, 922–927 (2018).
75. Ringe, E. Shapes, Plasmonic Properties, and Reactivity of Magnesium Nanoparticles. *J. Phys. Chem. C* **124**, 15665–15679 (2020).
76. Langer, J. *et al.* Present and Future of Surface-Enhanced Raman Scattering. *ACS Nano* **14**, 28–117 (2020).
77. Joo, S. W. & Kim, K. Adsorption of phenylacetylene on gold nanoparticle surfaces investigated by surface-enhanced Raman scattering. *J. Raman Spectrosc.* **35**, 549–554 (2004).
78. Jang, Y. H., Hwang, S., Oh, J. J. & Joo, S.-W. Adsorption change of cyclohexyl acetylene on gold nanoparticle surfaces. *Vib. Spectrosc.* **51**, 193–198 (2009).
79. Li, J., Liu, F., Bi, X. & Ye, J. Imaging immune checkpoint networks in cancer tissues with supermultiplexed SERS nanoprobes. *Biomaterials* **302**, 122327 (2023).
80. Shi, L. *et al.* Optical imaging of metabolic dynamics in animals. *Nat. Commun.* **9**, 2995 (2018).
81. Shea, D. A. & Morris, M. D. Bone Tissue Fluorescence Reduction for Visible Laser Raman Spectroscopy. *Appl. Spectrosc.* **56**, 182–186 (2002).
82. Asher, S. A., Johnson, C. R. & Murtaugh, J. Development of a new UV resonance Raman

spectrometer for the 217–400-nm spectral region. *Rev. Sci. Instrum.* **54**, 1657–1662 (1983).

83. Angel, S. M., DeArmond, M. K., Hanck, K. W. & Wertz, D. W. Computer-controlled instrument for the recovery of a resonance Raman spectrum in the presence of strong luminescence. *Anal. Chem.* **56**, 3000–3001 (1984).
84. De Luca, A. C., Mazilu, M., Riches, A., Herrington, C. S. & Dholakia, K. Online fluorescence suppression in modulated Raman spectroscopy. *Anal. Chem.* **82**, 738–745 (2010).
85. Friedman, J. M. & Hochstrasser, R. M. The use of fluorescence quenchers in resonance Raman spectroscopy. *Chem. Phys. Lett.* **33**, 225–227 (1975).
86. Bando, K. *et al.* Bessel-beam illumination Raman microscopy. *Biomed. Opt. Express* **13**, 3161–3170 (2022).
87. Mahadevan-Jansen, A. & Richards-Kortum, R. R. Raman spectroscopy for the detection of cancers and precancers. *J. Biomed. Opt.* **1**, 31–70 (1996).
88. Lewis, A. T. *et al.* Mirrored stainless steel substrate provides improved signal for Raman spectroscopy of tissue and cells. *J. Raman Spectrosc.* **48**, 119–125 (2017).
89. Lucotti, A. & Zerbi, G. Fiber-optic SERS sensor with optimized geometry. *Sensors Actuators, B Chem.* **121**, 356–364 (2007).
90. Smythe, E. J., Dickey, M. D., Jiming, B., Whitesides, G. M. & Capasso, F. Optical antenna arrays on a fiber facet for in Situ surface-enhanced Raman scattering detection. *Nano Lett.* **9**, 1132–1138 (2009).
91. Taylor, J. N. *et al.* Correction for Extrinsic Background in Raman Hyperspectral Images. *Anal. Chem.* **95**, 12298–12305 (2023).
92. Beier, B. D. & Berger, A. J. Method for automated background subtraction from Raman spectra containing known contaminants. *Analyst* **134**, 1198–1202 (2009).
93. Huang, J. *et al.* Extracting Optical Fiber Background from Surface-Enhanced Raman Spectroscopy Spectra Based on Bi-Objective Optimization Modeling. *Appl. Spectrosc.* **71**, 1808–1815 (2017).
94. Lieber, C. A. & Mahadevan-Jansen, A. Automated method for subtraction of fluorescence from biological Raman spectra. *Appl. Spectrosc.* **57**, 1363–1367 (2003).
95. Zhao, J., Lui, H., Mclean, D. I. & Zeng, H. Automated autofluorescence background subtraction algorithm for biomedical Raman spectroscopy. *Appl. Spectrosc.* **61**, 1225-1232 (2007).
96. Perez-Pueyo, R., Soneira, M. J. & Ruiz-Moreno, S. Morphology-Based Automated Baseline Removal for Raman Spectra of Artistic Pigments. *Appl. Spectrosc.* **64**, 595–600 (2010).
97. Liland, K. H., Almøy, T. & Mevik, B.-H. Optimal Choice of Baseline Correction for Multivariate Calibration of Spectra. *Appl. Spectrosc.* **64**, 1007–1016 (2010).
98. Guo, S., Bocklitz, T. & Popp, J. Optimization of Raman-spectrum baseline correction in

biological application. *Analyst* **141**, 2396–2404 (2016).

99. Fang, S. *et al.* Recent progress and applications of Raman spectrum denoising algorithms in chemical and biological analyses: A review. *TrAC Trends Anal. Chem.* **172**, 117578 (2024).
100. Ehrentreich, F. & Summchen, L. Spike removal and denoising of Raman spectra by wavelet transform methods. *Anal. Chem.* **73**, 4364–4373 (2001).
101. Člupek, M., Matějka, P. & Volka, K. Noise reduction in Raman spectra: Finite impulse response filtration versus Savitzky–Golay smoothing. *J. Raman Spectrosc.* **38**, 1174–1179 (2007).
102. Eilers, P. H. C. A perfect smoother. *Anal. Chem.* **75**, 3631–3636 (2003).
103. Barton, S. J., Ward, T. E. & Hennelly, B. M. Algorithm for optimal denoising of Raman spectra. *Anal. Methods* **10**, 3759–3769 (2018).
104. Chen, S. *et al.* Recovery of Raman spectra with low signal-to-noise ratio using Wiener estimation. *Opt. Express* **22**, 12102 (2014).
105. Gebrekidan, M. T., Knipfer, C. & Braeuer, A. S. Refinement of spectra using a deep neural network: Fully automated removal of noise and background. *J. Raman Spectrosc.* **52**, 723–736 (2021).
106. Kumamoto, Y., Li, M., Koike, K. & Fujita, K. Slit-scanning Raman microscopy: Instrumentation and applications for molecular imaging of cell and tissue. *J. Appl. Phys.* **132**, 171101 (2022).
107. Li, M. *et al.* Label-free chemical imaging of cytochrome P450 activity by Raman microscopy. *Commun. Biol.* **5**, 778 (2022).
108. Van Manen, H.-J. J., Kraan, Y. M., Roos, D. & Otto, C. Intracellular Chemical Imaging of Heme-Containing Enzymes Involved in Innate Immunity Using Resonance Raman Microscopy. *J. Phys. Chem. B* **108**, 18762–18771 (2004).
109. Hamada, K. *et al.* Raman microscopy for dynamic molecular imaging of living cells. *J. Biomed. Opt.* **13**, 044027 (2008).
110. Lee, Y. J., Moon, D., Migler, K. B. & Cicerone, M. T. Quantitative image analysis of broadband CARS hyperspectral images of polymer blends. *Anal. Chem.* **83**, 2733–9 (2011).
111. He, H. *et al.* Automated weak signal extraction of hyperspectral Raman imaging data by adaptive low-rank matrix approximation. *J. Raman Spectrosc.* **51**, 2552–2561 (2020).
112. Xu, J. *et al.* High-Speed Diagnosis of Bacterial Pathogens at the Single Cell Level by Raman Microspectroscopy with Machine Learning Filters and Denoising Autoencoders. *ACS Chem. Biol.* **17**, 376–385 (2022).
113. Machado, L. R. P. *et al.* Deep-learning-based denoising approach to enhance Raman spectroscopy in mass-produced graphene. *J. Raman Spectrosc.* **53**, 863–871 (2022).
114. Zeng, Y., Liu, Z., Fan, X. & Wang, X. Modified denoising method of Raman spectra-based deep learning for Raman semi-quantitative analysis and imaging. *Microchem. J.* **191**,

108777 (2023).

115. Byrne, H. J., Knief, P., Keating, M. E. & Bonnier, F. Spectral pre and post processing for infrared and Raman spectroscopy of biological tissues and cells. *Chem. Soc. Rev.* **45**, 1865–1878 (2016).
116. Borek-Dorosz, A. *et al.* Raman-based spectrophenotyping of the most important cells of the immune system. *J. Adv. Res.* **41**, 191–203 (2022).
117. Hislop, E. W., Tipping, W. J., Faulds, K. & Graham, D. Label-Free Imaging of Lipid Droplets in Prostate Cells Using Stimulated Raman Scattering Microscopy and Multivariate Analysis. *Anal. Chem.* **94**, 8899–8908 (2022).
118. Bonnier, F. & Byrne, H. J. Understanding the molecular information contained in principal component analysis of vibrational spectra of biological systems. *Analyst* **137**, 322–332 (2012).
119. Hill, I. E. *et al.* Understanding radiation response and cell cycle variation in brain tumour cells using Raman spectroscopy. *Analyst* **148**, 2594–2608 (2023).
120. Efeoglu, E., Casey, A. & Byrne, H. J. In vitro monitoring of time and dose dependent cytotoxicity of aminated nanoparticles using Raman spectroscopy. *Analyst* **141**, 5417–5431 (2016).
121. C. Fereidouni, F., Bader, A. N. & Gerritsen, H. C. Spectral phasor analysis allows rapid and reliable unmixing of fluorescence microscopy spectral images. *Opt. Express* **20**, 12729–41 (2012).
122. Murphy, N. *et al.* Expanding the Range of Bioorthogonal Tags for Multiplex Stimulated Raman Scattering Microscopy. *Angew. Chem. Int. Ed. Engl.* **62**, e202311530 (2023).
123. Fu, D. & Xie, X. S. Reliable Cell Segmentation Based on Spectral Phasor Analysis of Hyperspectral Stimulated Raman Scattering Imaging Data. *Anal. Chem.* **86**, 4115–4119 (2014).
124. Wei, M. *et al.* Volumetric chemical imaging by clearing-enhanced stimulated Raman scattering microscopy. *Proc. Natl. Acad. Sci. U. S. A.* **116**, 6608–6617 (2019).
125. Huang, K. C., Li, J., Zhang, C., Tan, Y. & Cheng, J. X. Multiplex Stimulated Raman Scattering Imaging Cytometry Reveals Lipid-Rich Protrusions in Cancer Cells under Stress Condition. *iScience* **23**, 100953 (2020).
126. Tipping, W. J. *et al.* Stimulated Raman scattering microscopy with spectral phasor analysis: applications in assessing drug-cell interactions. *Chem. Sci.* **13**, 3468–3476 (2022).
127. Hislop, E. W., Tipping, W. J., Faulds, K. & Graham, D. Label-Free Cytometric Evaluation of Mitosis via Stimulated Raman Scattering Microscopy and Spectral Phasor Analysis. *Anal. Chem.* **95**, 7244–7253 (2023).

128. Salic, A. & Mitchison, T. J. A chemical method for fast and sensitive detection of DNA synthesis in vivo. *Proc. Natl. Acad. Sci. U. S. A.* **105**, 2415–2420 (2008).
129. Cui, J. *et al.* Novel Raman-tagged sphingomyelin that closely mimics original raft-forming behavior. *Bioorg. Med. Chem.* **23**, 2989–94 (2015).
130. Katsir, L., Schilmiller, A. L., Staswick, P. E., He, S. Y. & Howe, G. A. COI1 is a critical component of a receptor for jasmonate and the bacterial virulence factor coronatine. *Proc. Natl. Acad. Sci. U. S. A.* **105**, 7100–5 (2008).
131. Egoshi, S. *et al.* Dual function of coronatine as a bacterial virulence factor against plants: possible COI1–JAZ-independent role. *RSC Adv.* **6**, 19404–19412 (2016).
132. Ueda, M. *et al.* Noncanonical Function of a Small-Molecular Virulence Factor Coronatine against Plant Immunity: An *In Vivo* Raman Imaging Approach. *ACS Cent. Sci.* **3**, 462–472 (2017).

This article is the first demonstration of ATRI to reveal the unknown mechanism of action of small bioactive molecules in living plant cells.

133. Ueda, M. *et al.* The alkyne-tag Raman imaging of coronatine, a plant pathogen virulence factor, in Commelina communis and its possible mode of action. *Org. Biomol. Chem.* **16**, 3348–3352 (2018).
134. Gaschler, M. M. *et al.* Determination of the Subcellular Localization and Mechanism of Action of Ferrostatins in Suppressing Ferroptosis. *ACS Chem. Biol.* **13**, 1013−1020 (2018).
135. Seidel. J. *et al.* Structure–activity–distribution relationship study of anti-cancer antimycin-type depsipeptides. *Chem. Commun.* **55**, 9379−9382 (2019)
136. Saito, Y. *et al.* Characterization of cellular uptake and distribution of coenzyme Q10 and vitamin E in PC12 cells. *J. Nutr. Biochem.* **20**, 350–357 (2009).
137. Zhang, Z. *et al.* Quantitative Evaluation of Surface-Enhanced Raman Scattering Nanoparticles for Intracellular pH Sensing at a Single Particle Level. *Anal. Chem.* **91**, 3254–3262 (2019).
138. Talarska, P., Boruczkowski, M. & Żurawski, J. Current Knowledge of Silver and Gold Nanoparticles in Laboratory Research—Application, Toxicity, Cellular Uptake. *Nanomaterials* **11**, 2454 (2021).
139. de Albuquerque, C. D. L., Sobral-Filho, R. G., Poppi, R. J. & Brolo, A. G. Digital Protocol for Chemical Analysis at Ultralow Concentrations by Surface-Enhanced Raman Scattering. *Anal. Chem.* **90**, 1248–1254 (2018).
140. Lin, L. *et al.* A bioorthogonal Raman reporter strategy for SERS detection of glycans on live cells. *Angew. Chem. Int. Ed Engl.* **52**, 7266–7271 (2013)

This article is the first demonstration of SERS-ATRI for showing the uptake and metabolism of small biomolecules in living cells.

141. Xiao, M. *et al.* SERS imaging of cell-surface biomolecules metabolically labeled with bioorthogonal Raman reporters. *Chem. Asian J.* **9**, 2040–2044 (2014).
142. Zhang, J. *et al.* In situ, accurate, surface-enhanced Raman scattering detection of cancer cell nucleus with synchronous location by an alkyne-labeled biomolecular probe. *Anal. Bioanal. Chem.* **410**, 585–594 (2018).
143. Makanai, H., Nishihara, T. & Tanabe, K. Surface-Enhanced Raman Scattering Identification of Nucleic Acid Targets by Acetylene-Tagged Hoechst Molecule Binding with DNA-Tethered Gold Nanoparticles. *ACS Appl. Nano Mater.* **5**, 2935–2942 (2022).
144. Makanai, H., Nishihara, T. & Tanabe, K. The pH-Dependent Raman Signal Enhancement of an Alkyne-tagged Hoechst Molecule that Binds with Oligodeoxynucleotides on Gold Nanoparticles. *Chem. Lett.* **51**, 1135–1138 (2022).
145. Chen, K. *et al.* A Background-Free SERS Strategy for Sensitive Detection of Hydrogen Peroxide. *Molecules* **27**, 7918 (2022).
146. Zhao, X. *et al.* Alkyne functionalized graphene-isolated-Au-nanocrystal for the ratiometric SERS sensing of alkaline phosphatase with acetonitrile solvent as an internal standard. *Sens. Actuators B Chem.* **331**, 129373 (2021).
147. Wang, F. *et al.* Self-Referenced Synthetic Urinary Biomarker for Quantitative Monitoring of Cancer Development. *J. Am. Chem. Soc.* **145**, 919–928 (2023).
148. El-Mashtoly, S. F. *et al.* Label-free imaging of drug distribution and metabolism in colon cancer cells by Raman microscopy. *Analyst* **139**, 1155–1161 (2014).
149. Sepp, K. *et al.* Utilizing Stimulated Raman Scattering Microscopy to Study Intracellular Distribution of Label-Free Ponatinib in Live Cells. *J. Med. Chem.* **63**, 2028–2034 (2020).
150. Tipping, W. J. *et al.* Temporal imaging of drug dynamics in live cells using stimulated Raman scattering microscopy and a perfusion cell culture system. *RSC Chem. Biol.* **3**, 1154–1164 (2022).
151. Tentellino, C. *et al.* Ratiometric imaging of minor groove binders in mammalian cells using Raman microscopy. *RSC Chem. Biol.* **3**, 1403–1415 (2022).
152. Tipping, W. J. *et al.* Ratiometric sensing of fluoride ions using Raman spectroscopy. *Chem. Commun.* **56**, 14463–14466 (2020).
153. Takemura, S., Watanabe, H., Nishihara, T., Okamoto, A. & Tanabe, K. Monitoring intracellular metal ion complexation with an acetylene-tagged ligand by Raman spectroscopy. *RSC Adv.* **10**, 36119–36123 (2020).

154. Romei, M. G. *et al.* Frequency Changes in Terminal Alkynes Provide Strong, Sensitive, and Solvatochromic Raman Probes of Biochemical Environments. *J. Phys. Chem. B* **127**, 85–94 (2023).
155. Bi, X., Miao, K. & Wei, L. Alkyne-Tagged Raman Probes for Local Environmental Sensing by Hydrogen-Deuterium Exchange. *J. Am. Chem. Soc.* **144**, 8504–8514 (2022).
156. Li, Y., Sun, Y. & Shi, L. Viewing 3D spatial biology with highly-multiplexed Raman imaging: from spectroscopy to biotechnology. *Chem. Commun.* **60**, 8658–8669 (2024).
157. Aljakouch, K. *et al.* Raman Microspectroscopic Evidence for the Metabolism of a Tyrosine Kinase Inhibitor, Neratinib, in Cancer Cells. *Angew. Chem. Int. Ed. Engl.* **57**, 7250–7254 (2018).
158. Feizpour, A., Marstrand, T., Bastholm, L., Eirefelt, S. & Evans, C. L. Label-Free Quantification of Pharmacokinetics in Skin with Stimulated Raman Scattering Microscopy and Deep Learning. *J. Invest. Dermatol.* **141**, 395–403 (2021).
159. Yamakoshi, H. *et al.* Simultaneous imaging of protonated and deprotonated carbonylcyanide p-trifluoromethoxyphenylhydrazone in live cells by Raman microscopy. *Chem. Commun.* **50**, 1341–1343 (2014).
160. Yamakoshi, H. *et al.* Ratiometric analysis of reversible thia-Michael reactions using nitrile-tagged molecules by Raman microscopy. *Chem. Commun.* **59**, 14563–14566 (2023).
161. Miao, Y., Qian, N., Shi, L., Hu, F. & Min, W. 9-Cyanopyronin probe palette for super-multiplexed vibrational imaging. *Nat. Commun.* **12**, 4518 (2021).
162. Min, W. & Gao, X. Fundamental detectability of Raman scattering: A unified diagrammatic approach. *J. Chem. Phys.* **160**, 094110 (2024).
163. Bi, X., Czajkowsky, D. M., Shao, Z. & Ye, J. Digital colloid-enhanced Raman spectroscopy by single-molecule counting. *Nature* **628**, 771–775 (2024).
164. Bi, X. *et al.* Digital colloid-enhanced Raman spectroscopy for the pharmacokinetic detection of bioorthogonal drugs. *Chem. Sci.* **15**, 13998–14008 (2024).
165. Khlebtsov, N. G., Lin, L., Khlebtsov, B. N. & Ye, J. Gap-enhanced Raman tags: Fabrication, optical properties, and theranostic applications. *Theranostics* **10**, 2067–2094 (2020).
166. Li, J., Liu, F., He, C., Shen, F. & Ye, J. Orthogonal gap-enhanced Raman tags for interference-free and ultrastable surface-enhanced Raman scattering. *Nanophotonics* **11**, 1549–1560 (2022).
167. Mizushima, K. *et al.*, Raman microscopy of cryofixed biological specimens for high-resolution and high-sensitivity chemical imaging. *Sci. Adv.* **10**, eadn0110 (2024).
168. Tipping, W. J., Lee, M., Serrels, A., Brunton, V. G. & Hulme, A. N. Imaging drug uptake by bioorthogonal stimulated Raman scattering microscopy. *Chem. Sci.* **8**, 5606–5615 (2017).

169. Pirali, T., Serafini, M., Cargnin, S. & Genazzani, A. A. Applications of Deuterium in Medicinal Chemistry. *J. Med. Chem.* **62**, 5276–5297 (2019).
170. Nishiyama, R. *et al.* Color-scalable flow cytometry with Raman tags. *PNAS nexus* **2**, pgad001 (2023).
171. Du, J. & Wei, L. Multicolor Photoactivatable Raman Probes for Subcellular Imaging and Tracking by Cyclopropenone Caging. *J. Am. Chem. Soc.* **144**, 777–786 (2022).
172. Ao, J. *et al.* Switchable stimulated Raman scattering microscopy with photochromic vibrational probes. *Nat. Commun.* **12**, 3089 (2021).
173. Shou, J. *et al.* Super-resolution vibrational imaging based on photoswitchable Raman probe. *Sci. Adv.* **9**, 1–10 (2023).
174. Tipping, W. J., Faulds, K. & Graham, D. Advances in Super-resolution Stimulated Raman Scattering Microscopy. *Chem. Biomed. Imaging* **2**, 733–743 (2024).
175. Gala De Pablo, J., Lindley, M., Hiramatsu, K. & Goda, K. High-Throughput Raman Flow Cytometry and beyond. *Acc. Chem. Res.* **54**, 2132–2143 (2021).
176. Kawagoe, H. *et al.* Multiwell Raman plate reader for high-throughput biochemical screening. *Sci. Rep.* **11**, 15742 (2021).

Glossary terms

alkyne tag: A detection tag consisting of alkyne, a small functional group made by carbon-carbon triple bond. An alkyne tag can be introduced into small compounds maintaining their original chemical and biological properties and produce a strong Raman signal in the cellular silent region, which can be visualized by Raman imaging.

Excitation cross-section: A measure of the probability that the excitation process will occur. In this case, a photon interacts with a molecule, transferring energy to excite it to a higher vibrational state. This interaction can result in Raman scattering.

Enhancement factor: How much a signal, such as Raman signal, is amplified under specific conditions compared to a standard condition.

Lysosomotropic: The property of compounds to accumulate in lysosomes, which are acidic compartments within cells.

RIE value: Relative Raman intensity versus 5-ethynyl-2'-deoxyuridine (EdU), which is calculated from the Raman spectrum of a mixture of test compound and EdU in DMSO solution.

Isotopic editing: Chemical modification of target compound by the substitution with stable isotopes.

multiplex detection: Simultaneous detection of multiple parameters within a single sample or experiment.

localised surface plasmon resonance: Phenomenon that occurs when metal nanoparticles, typically gold or silver, resonate with incident light at specific wavelengths leading to the enhancement of the electromagnetic field surrounding nanoparticles.

half-wave plate: An optical device that manipulates the polarization state of light. When light passes through the half-wave plate, its polarization state is rotated by an angle of 90 degrees.

optical modulator: A device that modulates properties of light waves, such as amplitude, phase, polarization, or frequency of light signals.

clusters (k): In machine learning and data analysis, data points are clustered together based on similarity or proximity. The parameter "k" represents the number of groups (clusters), indicating how many clusters the data is divided into.